http://dx.doi.org/10.1097/mm9.0000000000000035

MedMat

Original Research

OPEN

A two-stage nanoengineered microneedle platform for on-demand tumor-microenvironment-responsive therapy and enhanced wound healing against postoperative breast cancer recurrence

Yifan Fei[a], Xinhua Liu[a,*], Meilun Zhai[b], Xing Chen[a], Ouyang Yue[a], Xuechuan Wang[a], Huie Jiang[a,*], Yining Chen[c,*]

Abstract

Postoperative metastatic recurrence and wound infection pose significant threats to survival after breast cancer (BC) surgery. To address these challenges, an ideal therapeutic strategy should incorporate minimally invasive multifunctional biomaterials capable of simultaneously preventing tumor recurrence and promoting wound healing. Herein, we report a novel 2-stage microneedle (MN) platform engineered via the integration of nanotechnology and tumor-microenvironment-responsive design. This system is fabricated using a stepwise casting strategy and features tip-to-base architecture equipped with on-demand smart nanocarriers for synergistic therapy against postoperative BC recurrence and wound complications. The MN consists of a photo-crosslinked hydrogel tip encapsulating chitosan-based self-assembled nanocarriers and a gelatin–polydopamine hydrogel backing layer. Owing to its hierarchical structural design, the MN exhibits excellent mechanical strength with a compression force of up to 4.48 N per needle, sufficient for efficient skin penetration. Moreover, the platform demonstrates sustained pH-responsive behavior and specific tumor microenvironment targeting, enabling controlled drug release. The MN also displays outstanding biocompatibility and multifunctional therapeutic properties, including antibacterial adhesion, self-healing capability, swelling performance, and biodegradability, greatly broadening its potential as a precision medicine tool. Both in vitro and in vivo studies validated the robust and integrated therapeutic efficacy of the MN system in suppressing metastatic BC recurrence and enhancing infected wound healing. This work provides a significant advance in the design of smart 2-stage MNs with comprehensive functionality for minimally invasive adjuvant therapy after BC surgery.

Keywords: Breast cancer, Gelatin, Microneedle, Postoperative recurrence, Wound healing

1. Introduction

Breast cancer (BC) is the most prevalent malignancy among women worldwide[1,2]. Reports indicate that BC affects approximately 12% of women during their lifetime, with nearly 420,000 new diagnoses annually in China[3]. Surgical excision remains the standard intervention for primary BC[4]. However, a significant 10% to 40% risk of BC recurrence persists postsurgery[5–7]. Furthermore, severe local immune suppression, coupled with substantial wound infection and inflammation in postoperative patients, promotes cancer cell invasion and inhibits cellular activity. This further increases the incidence of BC recurrence and metastasis[8–10], ultimately leading to higher BC-related mortality. To prevent recurrence postsurgery, BC patients often undergo adjuvant chemotherapy, a systemic intervention that can substantially reduce local recurrence and mortality rates. Unfortunately, multidrug resistance[11] has emerged as a major challenge during chemotherapy, contributing to treatment failure in over 90% of patients. Moreover, conventional chemotherapeutic agents are cytotoxic, potentially harming normal cells and causing side effects such as myelosuppression, nausea, vomiting, and hair loss. Chemotherapy could also result in premature menopause, potentially increasing the risk of osteoporosis and impaired fertility[12,13]. Despite considerable advancements, a complete cancer cure and eradication remain elusive. Additionally, the risks of surgical infections and increased susceptibility to bacterial infections due to weakened immunity following tumor surgery can lead to life-threatening complications[14,15]. Given these diverse clinical postoperative challenges, conventional cancer treatments are often insufficient for meeting the complex, multifactorial requirements of postoperative tumor management[16]. Therefore, developing an intelligent adjuvant therapeutic strategy is imperative to prevent tumor recurrence and potential wound infections following tumor resection.

Emerging local administration methods that increase drug concentration at target sites while minimizing harmful side

[a]College of Bioresources Chemical and Materials Engineering, Shaanxi University of Science &Technology, Xi'an, China, [b]Department of Plastic Surgery, The First Affiliated Hospital, School of Medicine, Zhejiang University, Hangzhou, China, [c]College of Bioresources Science and Engineering, Sichuan University, Chengdu, China.

*Corresponding authors: Address: Xinhua Liu, College of Bioresources Chemical and Materials Engineering, Shaanxi University of Science &Technology, Xi'an 710021, China. E-mail address: liuxinhua@sust.edu.cn (Xinhua Liu); Yining Chen, College of Bioresources Science and Engineering, Sichuan University, Chengdu 610065, China. E-mail address: chenyining@scu.edu.cn (Yining Chen); Huie Jiang, College of Bioresources Chemical and Materials Engineering, Shaanxi University of Science &Technology, Xi'an 710021, China. E-mail address: jianghuie@sust.edu.cn (Huie Jiang).

Supplemental Digital Content is available for this article.

MedMat (2026) 3:1

Received: 29 August 2025; Accepted 2 December 2025

Published online xxx xx 2026

effects and simplifying application have recently attracted significant research interest. Topical drug delivery systems—including hydrogels[17], micelles[18], liposomes[19], nanoparticles (NPs)[20], and microneedles (MNs)[21], demonstrate potential for reducing toxicity to healthy tissues and enhancing therapeutic efficacy. As a next-generation drug delivery platform[22], on-demand engineered MNs have gained widespread popularity. Compared to traditional transdermal systems, MN-based delivery easily penetrates the stratum corneum, bypasses the skin barrier, and creates micropores in the epidermis. Furthermore, the capillary action within these micropores significantly enhances drug permeability and penetration across skin layers[23,24]. Moreover, MN-delivered drugs avoid dilution in the bloodstream and first-pass hepatic metabolism by the liver, as they directly enter local tissues, substantially accumulating in target sites. This increases drug utilization, resulting in more sustained therapeutic effects and reduced systemic toxicity[25,26]. Significant biomedical engineering advancements have been realized in MN transdermal technologies[27–29]. Specifically for BC patients[30], MNs enable relatively noninvasive drug delivery, allowing precise drug level regulation in breast tissue based on body weight, tumor size, and drug recycling time[31], thereby mitigating the negative effects of conventional oral or systemic drug administrations. MN therapy for BC can also significantly reduce pain during tumor detection and drug injection, enable the codelivery of multiple drugs, and achieve spatiotemporal drug-release control[32]. Although MN technology and its application in treating other cancers have been extensively investigated[33–36], developing MN arrays for BC recurrence treatment remains challenging. This is primarily because suppressing postoperative recurrence and metastasis is a critical focus of BC management. Notably, simple drug loading and delivery via MNs can result in rapid release, limiting sustained delivery necessary for long-term suppression of cancer cell recurrence[37].

From a therapeutic perspective, ideal MNs for BC therapy should not only suppress local area recurrence and potential wound infections but also stimulate tissue repair. In other words, new-generation MNs require subtle intelligence based on the tumor microenvironment (TME), adequate penetration capability, biocompatibility, tissue regeneration potential, and integrated therapeutic effects combining antitumor and antibacterial activities. Beyond the advantages of traditional transdermal technologies, emerging 2-stage MNs, typically comprising a support base and a degradable MN tip, offer unique properties reportedly superior to other MN modalities. These include enhanced efficiency, stability, biosafety, and bioavailability[38,39]. However, the current MNs used in BC treatment demonstrate limitations, such as skin allergies and reduced drug penetration due to local accumulation[40–42]. In contrast, the solid lower-stage structure of 2-stage MNs provides inherent mechanical strength. This facilitates effective skin penetration and allows separation of the drug-carrying soluble upper stage from the lower base, improving drug utilization and delivery precision. Two-stage MN thus offer the dual advantages of subcutaneous administration and skin patching for BC. Nonetheless, versatile MNs specifically designed for BC treatment remain scarcely reported.

Herein, we developed a drug delivery system integrating novel 2-stage MNs and nanocarriers to enhance transdermal drug transport. We combined nanotechnology and stimuli-responsive strategies to engineer a multifunctional "smart-response" MN platform for diverse therapeutic effects against BC recurrence and wound infection, while also promoting wound healing (Figure 1). Figure 1A illustrates the 2-stage MN structure. Its tip comprises a photo-crosslinked hydrogel containing chitosan-based self-assembled nanocarriers. Through the ionic-crosslinking assembly, the tip forms pH-responsive chitosan nanoparticle drug carriers (CS-β-CD NPs). Crucially, CS-β-CD NPs remain stable under neutral conditions but rapidly disintegrate in weakly acidic environments, enabling long-term pH-responsiveness and specific TME recognition, thus resulting in targeted doxorubicin (DOX) release (Figure 1B). The MN base comprises a gelatin-dopamine hydrogel, providing effective tissue puncture, drug delivery, tissue adhesion, and self-healing properties. Furthermore, the MN demonstrated good biosafety and exerted antimicrobial therapeutic effects via polymyxin and basic fibroblast growth factor (bFGF) release, inhibiting tissue infection and accelerating wound healing (Figure 1C). Therefore, in postoperative BC management, our MN significantly inhibits BC recurrence and metastasis while reducing the toxic side effects of anticancer medications like DOX. Simultaneously, it facilitates tissue repair. This 2-stage MN intervention presents a novel approach for preventing postoperative BC metastasis and recurrence, deterring wound infections, and promoting wound healing.

2. Results and discussion

2.1 Synthesis and characterization of CS-β-CD NPs

Figure 2A illustrates the synthesis pathway for chitosan (CS) grafted with β-cyclodextrin (CS-β-CD). Specifically, 1-(3-dimethylaminopropyl)-3-ethylcarbodiimide/N-hydroxysuccinimide activated the carboxyl group of carboxymethyl-β-cyclodextrin (CMCD), which reacted with the amino group on the CS chain, yielding a CMCD-modified CS. According to the Fourier transform infrared spectroscopy (FTIR) results (Figure 2B), CS exhibited a characteristic peak of the amide I band at 1641 cm^{-1}, attributable to the C=O stretching vibration. On the other hand, the amide II band showed a characteristic peak at 1574 cm^{-1}, reflecting the plane-bending vibration of the N-H bond. At the same time, the vibrational peak of the amino group was observed at 1155 cm^{-1}. Compared to CS, the amide peak position of CS-β-CD showed a slight redshift with a significantly enhanced signal, potentially attributable to the formation of a new amide bond between the amino and carboxyl groups of CS and CMCD, respectively. Furthermore, CS-β-CD showed a carboxymethyl absorption peak near 1416 cm^{-1}, corresponding to the carboxymethyl group derived from CMCD. According to the X-ray diffraction (XRD) results (Figure 2C), CS exhibited a strong crystalline peak at about 20 °, indicating that it mainly exists in the form of type II crystals. Furthermore, the crystalline peaks of CMCD appeared at about 20 ° and 10 °, indicating that it contains both type I and type II crystals, with the latter being slightly more frequent. Conversely, the XRD image of CS-β-CD revealed that the diffraction peaks of type II crystals were significantly broader compared to those of CS. Additionally, the XRD map of CS-β-CD revealed that the diffraction peaks of type II crystals were significantly broader than those of CS, almost covering the entire region of the diffraction peaks of type II crystals in both CS and CMCD. It is also noteworthy that the crystallographic diffraction peaks of CS-β-CD were more shifted compared to those of CMCD, indicating that introducing CMCD not only somewhat maintained the original ordered structure of CS but also altered the order of part of the CS structure, generating a new ordered structure.

Herein, CS-β-CD NPs were successfully prepared through the ionic-crosslinking method. During synthesis, the negatively charged TPP interacted with the positively charged CS chains in CS-β-CD (Figure 2A). To determine the most suitable mixing ratio of CS-β-CD and TPP solutions for constructing CS-β-CD NPs with the most suitable particle size, 5 different ratios of CS-β-CD to TPP solutions (2:1, 3:1, 4:1, 5:1, and 6:1) (Figure 2D) were prepared. Particle sizes at different ratios were then characterized using a nanoparticle size analyzer. The average particle size gradually increased with the amount of TPP added dropwise (Figure 2E). As the volume ratio of CS to TPP decreased, the Zeta potential of CS-β-CD NPs decreased from

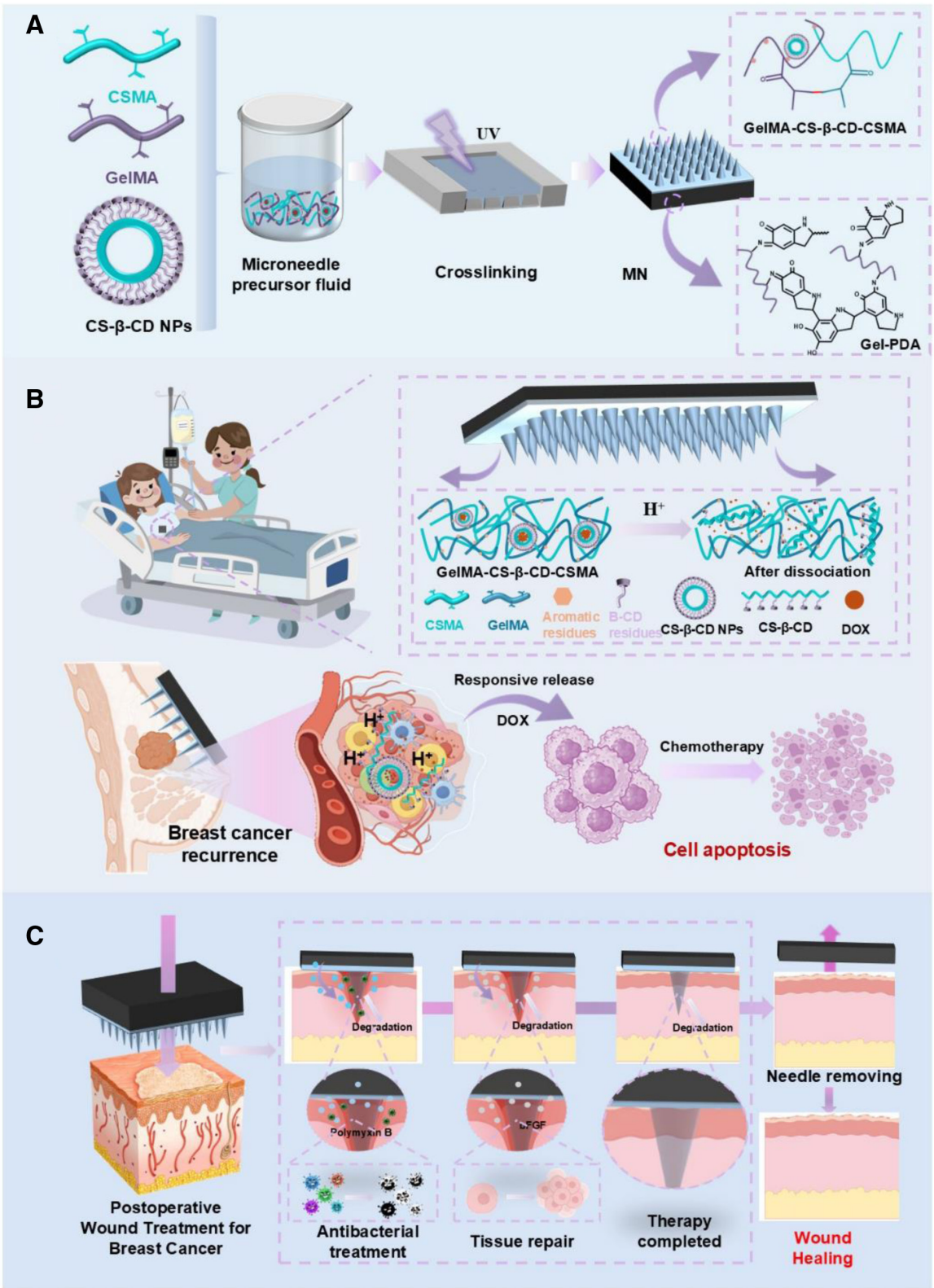

Figure 1. Mechanism of action and application of microneedles. (A) Schematic diagram of MN. (B) Mechanism of anticancer action of MN. (C) Mechanism of tissue repair of MN.

+ 25.71 to + 15.23 mV (Figure 2F). This trend is attributed to the increased TPP concentration, which promotes ion crosslinking between phosphate groups and protonated amino groups, resulting in larger NPs and more hydrogen bonding between molecules, thereby increasing particle size and decreasing zeta potential. Furthermore, scanning electron microscopy (SEM) and transmission electron microscopy (TEM) images (Figure 2J, K) revealed that at low magnification, CS-β-CD NPs exhibited aggregated particle morphology with a relatively uniform size distribution. At higher magnification, dispersed CS-β-CD NPs

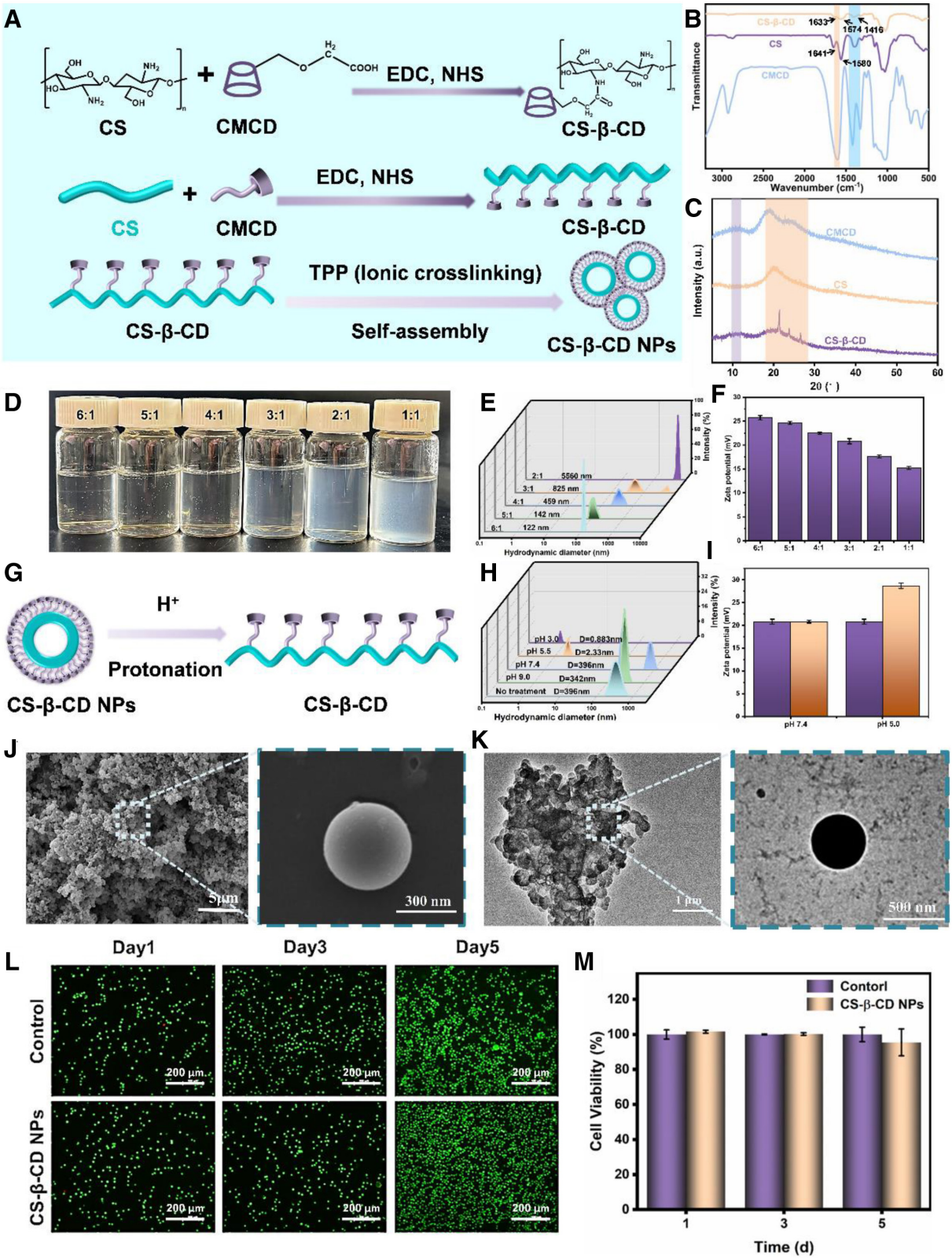

Figure 2. Preparation and characterization of CS-g-CD NPs. (A) Diagram of the synthesis mechanism of CS-β-CD and CS-β-CD NPs. (B) FTIR spectra of CS, CMCD, and CS-β-CD. (C) XRD spectra of CS, CMCD, and CS-β-CD. (D) CS-β-CD NPs solutions were prepared with different CS/TPP mass ratios (6:1, 5:1, 4:1, 3:1, 2:1, 1:1). (E) The particle size distribution of CS-β-CD NPs with different CS/TPP mass ratios (6:1, 5:1, 4:1, 3:1, 2:1, 1:1). (F) Zeta potential of CS-β-CD NPs with different CS/TPP mass ratios (6:1, 5:1, 4:1, 3:1, 2:1, 1:1). (G) Dissociation diagram of CS-β-CD NPs pH-sensitive. (H) Stability analysis of CS-β-CD NPs in different pH (1.0, 5.5, 7.4, 9.0) and culture media. (I) Zeta potential of CS-β-CD NPs treated with different pH (7.4, 5.0). (J, K) SEM and TEM images of CS-β-CD NPs. (L) Photomicrographs of the cell density of the MTT test of the control and CS-β-CD NPs for 5 days. (M) The cell viability of control and CS-β-CD NPs were cocultured with cells for 5 days. Data are depicted as mean ± SD (n = 3) and analyzed by one-way ANOVA with Tukey's multiple comparison test compared to the control group. ANOVA, analysis of variance.

appeared as spherical NPs approximately 450 nm in diameter, consistent with the particle size analysis results.

In order to investigate the stability and pH responsiveness of CS-β-CD NPs, herein, CS-β-CD NPs were dispersed in PBS at pH values of 3.0, 5.5, 7.4, and 9.0 to explore their pH responsiveness. Changes in particle size were then measured using a dynamic light scattering particle size analyzer. According to the results (Figure 2H, I), the NPs maintained their original size at pH values of 7.4 and 9.0, indicating the stability of CS-β-CD NPs under slightly and moderately alkaline conditions. Conversely, the original peaks disappeared at pH values of 5.5 and 3.0, and new peaks with smaller size ranges appeared, suggesting that CS-β-CD NPs disintegrated under acidic conditions before decomposing into larger molecular chains. This outcome could be attributed to TPP protonates losing their negative charge under acidic conditions, leading to the dissolution of the crosslinked structure between TPP and CS and NP breakdown into large molecular chains (Figure 2G) Therefore, CS-β-CD NPs could be widely used in nano-loaded drug delivery systems for acidic TMEs.

The cytotoxicity of blank CS-β-CD NPs was evaluated by the HeLa cell line and the HUVEC cell line, respectively. Supplementary Figure 2, https://links.lww.com/MEDMAT/A8 shows the survival of HeLa cells (A) and HUVEC (B) treated with different concentrations of CS-g-CD NP for 48 hour. In the concentration range of 1–200 μg/mL, the survival rate of HeLa cells treated with CS-g-CD NP was more than 80 %, and the survival rate of HUVEC was more than 90%. The results of cell proliferation/death experiments showed that red cells did not appear after the introduction of CS-β-CD NPs (the surviving cells were green and the dead cells were red) (Figure 2L), indicating that CS-β-CD NPs did not cause cytotoxicity 5 days later, the number of surviving cells became more, which proved that CS-β-CD NPs could promote cell proliferation (Figure 2M).

2.2 Preparation of GelMA and CSMA

By improving the method reported in the literature, methacrylated gelatin (GelMA) and methacryloylated chitosan (CSMA) were successfully synthesized (Figure 3A, B). A supramolecular hydrogel tip matrix, GelMA-CS-β-CD-CSMA, composed of GelMA, CSMA, and CS-β-CD NPs, was then prepared (Figure 3C). Upon adding the dispersed CS-β-CD NP solution into the mixed solution containing aromatic amino acids, the gel incorporated amino acids such as tyrosine, phenylalanine, and tryptophan. These aromatic amino acids subsequently infiltrated the β-cyclodextrin cavity, forming host–guest inclusion complexes. Figure 3E shows the proton nuclear magnetic resonance (^{1}H NMR) spectra of GelMA and CSMA. In GelMA, peak "a" represents the proton signals of aromatic amino acid residues in gelatin. In contrast, peak "b" corresponds to distinct signals at 5.62 and 5.48 ppm, attributed to the hydrogen peaks of the MA's C=C double bond[43,44], indicating successful grafting of MA onto the gelatin molecular chain. Furthermore, the ^{1}H NMR spectrum of CSMA exhibited peaks at chemical shifts of 1.84, 1.92, 2.9, and 3.2–3.9 ppm, corresponding to the methyl protons of MA residues, methyl protons on CS sugar, acetyl-amino protons on CSMA sugar, and sugar ring protons on CSMA, respectively. It is also noteworthy that the chemical shift at 4.7 ppm corresponds to the proton peak of D_2O, while those at 5.49 and 5.58 ppm correspond to the 2 proton peaks of the MA C=C bond (Figure 3D)[45]. Each material's infrared spectra are presented in Figure 3D. In the FTIR spectrum of GelMA, the absorption peaks at 3483 cm^{-1} corresponded to the N-H and O-H stretching vibrations, whereas the absorption peak at 1645 cm^{-1} corresponded to the stretching vibration of the C=C bond in the amide I band. Furthermore, the absorption peak at 1550 cm^{-1} corresponded to N-H bending vibration in the amide II band, implying an interaction between amino groups in gelatin molecules and MA through methyl acrylate ester units[46,47]. In the FTIR spectrum of CSMA, the telescopic vibrational absorption peak of $-NH_2$ at 1699 cm^{-1} disappeared. Furthermore, the absorption peaks at 3319, 1642, and 1445 cm^{-1} corresponded to the telescopic vibrational peaks of N-H and O-H, telescopic vibrational peaks of the amide I band with the C=C bond, bending vibrational peaks of the amide II band with the N-H bond, and characteristic absorption peak of the amide III band, respectively[48]. In summary, the disappearance of the $-NH_2$ absorption peak and formation of a characteristic peak of the amide bond indicate that MA was successfully acylated with the amino group of CS and grafted onto the CS molecular chain. Finally, in FTIR GelMA-CS-β-CD-CSMA spectra, a carboxymethyl absorption peak was observed at 1416 cm^{-1}, which originated from CMCD.

The results of the traditional inverted tube method showed that the GelMA-CS-β-CD-CSMA aqueous solution had photocuring gelation properties, that is, under ultraviolet light irradiation, GelMA-CS-β-CD-CSMA formed a supramolecular hydrogel (Figure 3F). Figure 3G shows the cross-section morphology of GelMA-CS-β-CD-CSMA. It can be seen from the figure that its interior is a loose porous structure, which can provide a convenient transmission channel for nutrients, making it easier for cells to adhere, grow, and migrate inside the hydrogel. Moreover, based on the rheological behavior graph (Figure 3H), the G′ (energy storage modulus) values of the 4 materials were greater than the respective G″ (loss modulus) values, indicating that the samples formed a stable gel compound. Furthermore, the MN had a larger G′ value, indicating that it resulted in a more stable network structure with a strong mechanical strength. This outcome could be attributed to the fact that the strain capacity of the final MN significantly improved with the continuous modification and crosslinking of the Gel and the addition of the Gel-PDA substrate part, resulting in a more stable structure.

2.3 Preparation and morphological characterization of MN

Figure 4A shows the MN preparation process. Herein, polydimethylsiloxane (PDMS) MN molds were utilized for the preparation of MNs in 4 steps: (1) First, the GelMA-CS-β-CD-CSMA solution was vacuum-filled into PDMS molds and exposed to UV light for gelation (Figure 4Ai); (2) second, the solution was naturally dried to form a needle tip structure (Figure 4Aii); (3) third, the Gel-PDA solution was added as a backing material through vacuum-assisted application (Figure 4Aiii); and (4) finally, the Gel-PDA solution was naturally dried and demolded to obtain 2-ended MN products (Figure 4Aiv).

To observe the morphology of the MNs, they were characterized using SEM, confocal laser scanning microscopy (CLSM), and super depth of field microscopy. Figure 4B depicts a macroscopic and microscopic view of an intact MN comprising 10 × 10 circular MNs with a conical tip portion and tip distance of ~500 μm. The tip portion of the MN was not clearly demarcated from the basal portion, indicating that the 2 portions were well connected. Under the bright-field image of the microscope, a uniformly arranged array of conical spikes in the MN can be observed (Figures 4Ci). To more effectively visualize the distribution of DOX within the MNs, the red dye rhodamine B (RhB) was added to GelMA-CS-β-CD-CSMA to simulate the drug. RhB was observed to be tightly attached to the MNs (Figure 4Ciii). To illustrate the MN's 2-stage structure, DOX was simulated using RhB and examined with a super depth-of-field microscope. The MN exhibited a distinct 2-part structure (Figure 4Cv): a tip (red; height = 800 μm) and a base (thickness = 200 μm). Additionally, three-dimensional (3D) imaging (Figure 4Cvi) and cross-sectional views (Figure 4D) obtained via laser confocal microscopy revealed a uniform and continuous red fluorescence in the outer layer of the MN + RhB. Overall, these results demonstrate the successful fabrication of the GelMA-CS-β-CD-CSMA drug-loaded tip and its integration

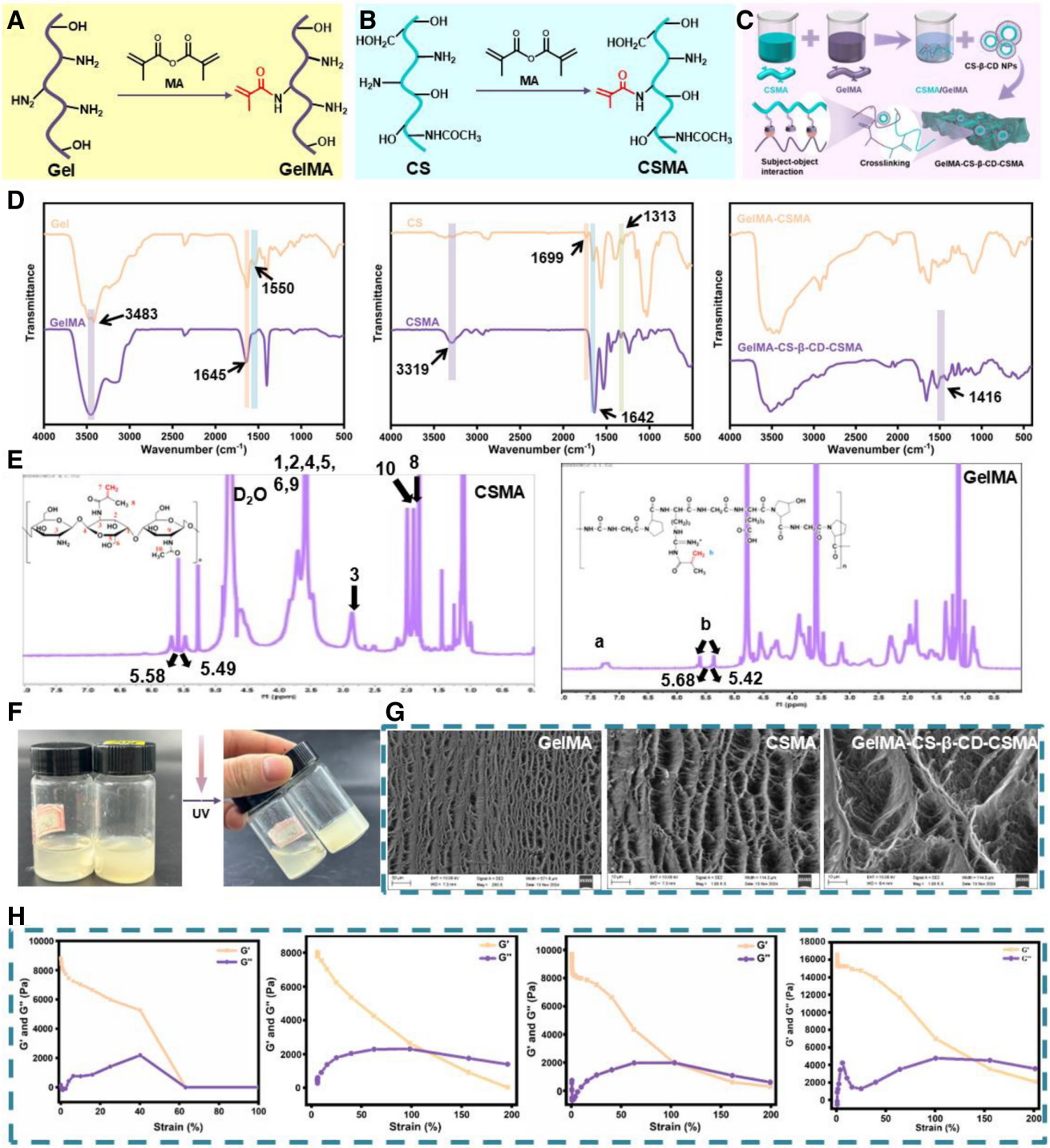

Figure 3. Preparation and characterization of GelMA-CS-β-CD-CSMA. (A) Synthetic reaction mechanism of GelMA. (B) Synthetic reaction mechanism of CSMA. (C) Synthetic reaction mechanism of GelMA-CS-β-CD-CSMA. (D) FTIR spectras of Gel and GelMA, CS and CSMA, GelMA-CSMA, and GelMA-CS-β-CD-CSMA. (E) ^{1}H NMR spectra of GelMA and CSMA. (F) Optical display diagram of gelling by inverted bottle method of GelMA-CS-β-CD-CSMA. (G) SEM images of GelMA, CSMA, and GelMA-CS-β-CD-CSMA. (H) Rheological behavior profiles of Gel, GelMA-CS-β-CD, GelMA-CS-β-CD-CSMA, and MN. Data are depicted as mean ± SD (n = 3) and analyzed by one-way ANOVA with Tukey's multiple comparison test compared to the control group.

with the Gel-PDA base to form a 2-part MN. This structural design reduces drug wastage commonly associated with conventional 1-piece MNs.

2.4 Performance characterization of the MNs

To verify the puncture performance of the MN, an MN patch loaded with Rh B was pierced into the skin tissue of depilated rats. The superficial layer of the skin exhibited regular red dimples (Figure 5A). Subsequently, this skin tissue was processed by freezing, sectioning, and paraffin embedding before observation via CLSM. The results (Figure 5A) confirmed that the MNs were successfully embedded into the rat skin, showing uniform puncture point spacing and clear puncture depth. Moreover, the red RhB localized in the deeper skin layers showed minimal diffusion, indicating that the UV-cured crosslinked 3D

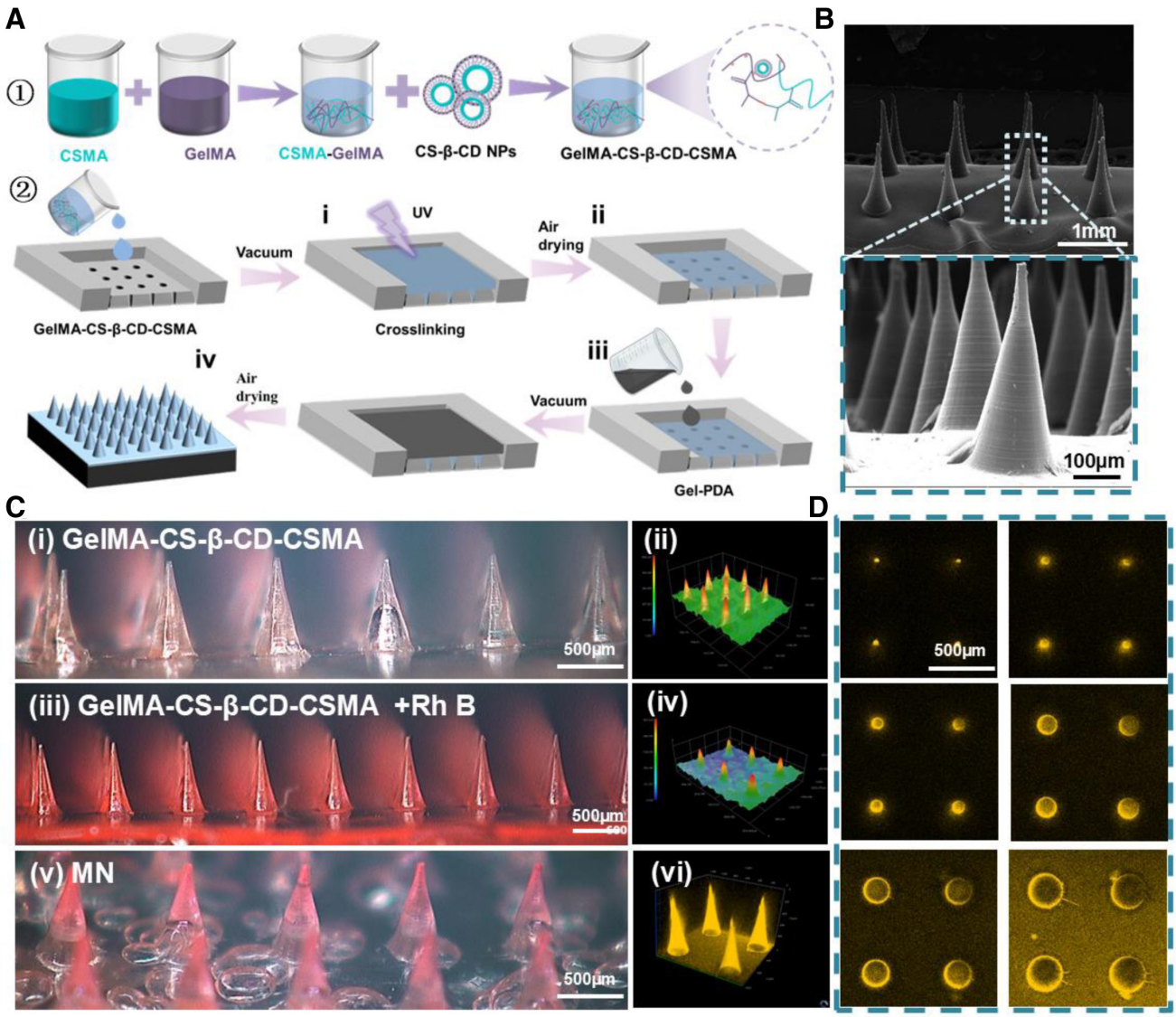

Figure 4. Preparation and morphological characterization of MN. (A) Schematic illustration of MN preparation. (B) SEM image of MN. The above image is the overall morphology, and the following image is locally enlarged. (C) Brightfield micrographs (i, iii, and v), three-dimensional height map images (ii and iv), and (vi) laser confocal fluorescence microscope image of GelMA-CS-β-CD-CSMA, GelMA-CS-β-CD-CSMA+Rh B and MN. (D) Laser confocal fluorescence microscope cross-sections of MN. Data are depicted as mean ± SD (n = 3) and analyzed by one-way ANOVA with Tukey's multiple comparison test compared to the control group.

mesh structure limited tissue fluid penetration and inhibited fluorescent dye diffusion. This suggests that osmotic pressure could facilitate the slow release of the drug after the MNs loaded with the drug are inserted into the skin tissue. Next, the mechanical properties of the MNs were characterized using a universal testing machine to determine their ability to penetrate the stratum corneum (Supplementary Figure 1, https://links.lww.com/MEDMAT/A8). The stress-strain curves (Figure 5B) demonstrated GelMA, synthesized by modifying gelatin macromolecular chains with MA and crosslinked via UV curing, exhibited improved mechanical properties due to the dense network structure formed by the crosslinked molecular chains. Although the GelMA-CS-β-CD and GelMA-CS-β-CD-CSMA complexes, obtained through further crosslinking with CS-β-CD NPs and GelMA, could withstand increased pressure, they were prone to fracture under large strains. The addition of a Gel-PDA gel matrix significantly enhanced the strain capacity and compressive strength of the MN, greatly improving their mechanical properties. Consequently, the MN could endure substantial strain without fracturing under higher pressure (Supplementary Figure 2, https://links.lww.com/MEDMAT/A8). As shown in Supplementary Figure 3, https://links.lww.com/MEDMAT/A8, the maximum stress achieved was 4.48 N/needle, which fully meets the stress requirements for skin puncture[49,50]. To evaluate the mechanical properties of the MN under humid conditions, compression tests were conducted in a hydrated environment. As shown in Figure 5C, the compressive force of the MNs increased with strain in both dry and wet environments; however, the mechanical performance under dry conditions was significantly superior to that under wet conditions. This discrepancy can be attributed to the swelling of the MN material and the disruption of hydrogen bonding networks caused by moisture in the wet environment, leading to a reduction in compressive modules and mechanical strength. Nevertheless, even under wet conditions, the compressive force continued to rise with increasing strain, and the maximum compressive force sustained by the MNs reached 100 N (equivalent to 1 N/needle) (Supplementary Figure 4, https://links.lww.com/MEDMAT/A8). This demonstrates that the MNs can provide effective penetration force within the strain range required for stratum corneum puncture.

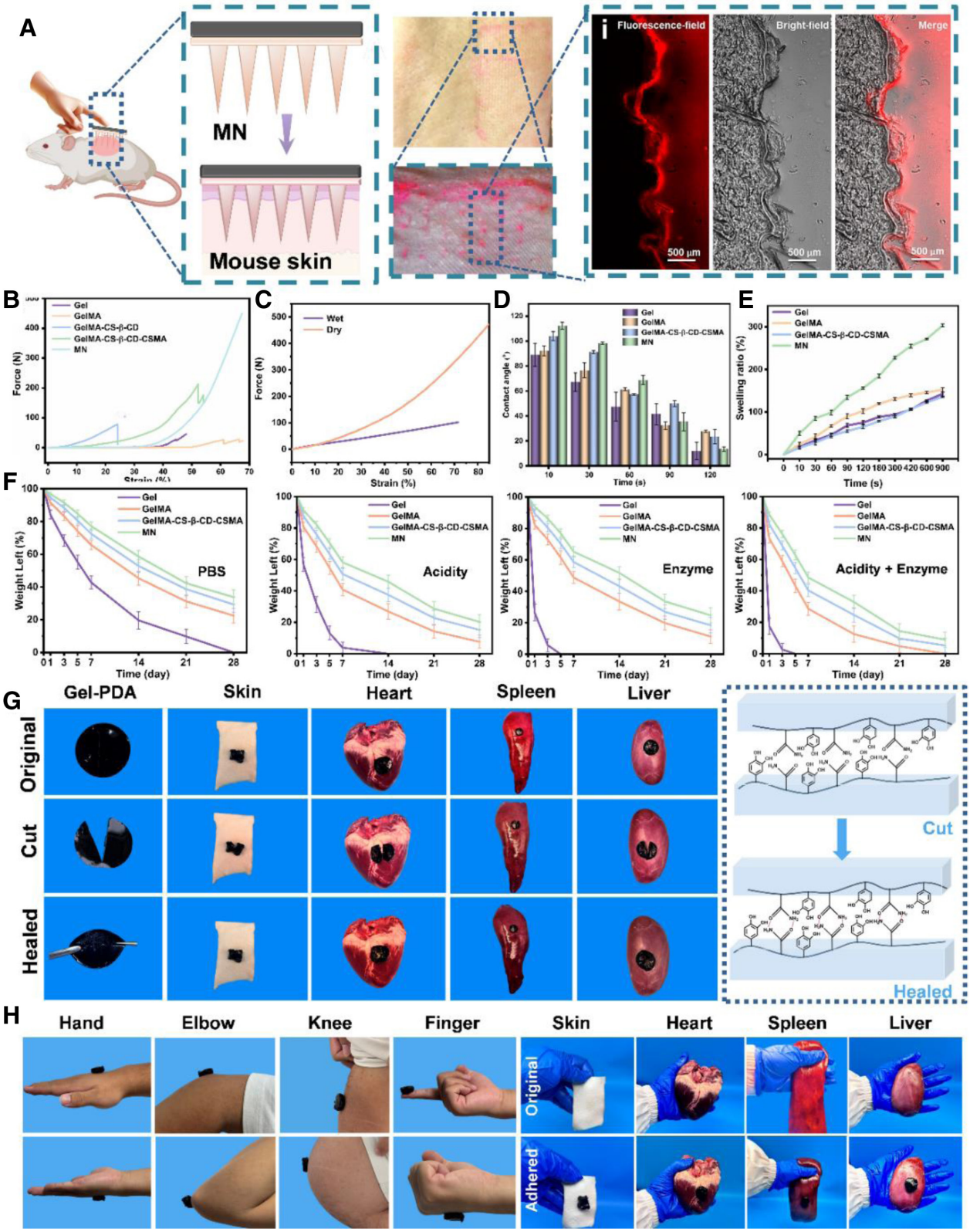

Figure 5. Basic properties of MN. (A) Schematic diagram of MN puncture into the skin with MN acting on the skin tissue, fluorescence imaging map of the thickness of MN puncture into the skin tissue (i). (B) Stress-strain curves of Gel, GelMA, GelMA-CS-β-CD, GelMA-CS-β-CD-CSMA, and MN. (C) The force-strain curves of MN in wet and dry states. (D) Contact angle test results of Gel, GelMA, GelMA-CS-β-CD-CSMA, and MN. (E) Test results of swelling properties of Gel, GelMA, GelMA-CS-β-CD-CSMA, and MN. (F) The weight retention rate of Gel, GelMA, GelMA-CS-β-CD-CSMA, and MN in different environments (PBS, acid, enzyme, acid+enzyme) on the 1, 3, 5, 7, 14, 21, and 28th day. (G) Self-healing properties of Gel-PDA in skin, heart, spleen and liver and the schematic diagram of repair. (H) Adhesion effect of Gel-PDA on human hands, elbows, knees, fingers and in vitro skin, heart, spleen and liver. Data are depicted as mean ± SD (*n* = 3) and analyzed by one-way ANOVA with Tukey's multiple comparison test compared to the control group.

According to the contact angle results (Figure 5D and Supplementary Figure 5, https://links.lww.com/MEDMAT/A8), the droplets in each material showed good penetration attributable to the large number of carboxyl and amino groups in the Gel, making the materials highly hydrophilic (ie, good wettability and liquid absorption). Notably, the MN's dissolution speed will directly affect the drug diffusion rate from the MN to the surrounding area. According to the dissolution characterization results (Figure 5E), the dissolution rates increased with time. However, its swelling rate was relatively slow, which led to slow dissolution during tissue fluid infiltration, delaying DOX release and preventing sudden release. Furthermore, to assess the swelling state of the MN in vivo, the skin tissue was simulated using agarose gel and MN was injected into the agarose. Compared to the initial state of the MN, after it was injected into the agar, the aqueous solution therein infiltrated the MN hydrogel network, increasing the MN's volume. Although the MN's increased volume resulted in an apparent expansion change, the MN retained its intact conical structure (Supplementary Figure 6, https://links.lww.com/MEDMAT/A8), which would facilitate the continuous release of the drug in the MN into the tissue fluid.

To systematically evaluate the degradation behavior of the MN tip materials developed in this study, we prepared Gel, GelMA, GelMA-CS-β-CD-CSMA, and MN samples and conducted a 28-day in vitro degradation study under both simulated physiological conditions (PBS, pH 7.4) and a simulated post-tumor resection complex microenvironment (pH 6.8+enzymes). As shown in Figure 5F, all 4 materials exhibited expected degradation trends in PBS (pH 7.4). Pure gelatin MNs, lacking a crosslinked network, degraded rapidly primarily through a dissolution mechanism, with the mass remaining dropping to (42.8% ± 3.8%) within 7 days, indicating their unsuitability for long-term drug delivery. In contrast, GelMA, due to its stable 3D network formed by photo-initiated crosslinking, demonstrated excellent resistance to dissolution, retaining a high mass remaining of (24.7% ± 3.5%) after 28 days (Supplementary Figure 7, https://links.lww.com/MEDMAT/A8). However, under the composite environment (pH 6.8+enzymes), the degradation behaviors of the 4 materials diverged significantly. Gel was rapidly disintegrated by the enzymatic action of collagenase, degrading (97.3% ± 4%) within just 3 days. Although GelMA could withstand acidic dissolution alone, it remained susceptible to enzymatic attack, degrading significantly faster than in PBS and being almost completely degraded by day 28 (Supplementary Figure 8, https://links.lww.com/MEDMAT/A8). Notably, while the MN, due to its crosslinked network, exhibited relatively good degradation resistance, it still degraded by approximately 90% over 28 days (Supplementary Figure 7, https://links.lww.com/MEDMAT/A8). This is attributed to the protonation of amine groups on the chitosan chains under acidic conditions, leading to their dissolution and leaching from the gel network, which disrupts the material's microstructure and creates numerous pores and channels. Consequently, collagenase can penetrate more deeply into the compromised network, accelerating the enzymatic degradation of the GelMA backbone. This synergistic effect of acid and enzyme enables the MN composite to respond actively to the pathological microenvironment, establishing a solid foundation for targeted and sustained drug release. Figure 5G systematically reveals the self-healing properties of gelatin dopamine hydrogels from the macro-morphology and micro-molecular action levels: macroscopically, the broken interface fused and recovered the mechanical load-bearing capacity (Cut) within 24h after physically cutting the Gel-PDA hydrogel (Original). Whether it is Gel-PDA's own material ("Cut" column), or on the surface of biological tissues such as skin, heart, spleen, and liver, after cutting treatment, Gel-PDA can achieve effective recovery of structural integrity in the "Healed" stage, reflecting the universality of its self-healing properties. Microscopically, the molecular structure of the cut state (Healed) showed that the external force destroys the catechol moiety of dopamine and gelatin. The molecular structure of the cut state (Cut) reveals that external forces break the hydrogen bonds and weak covalent bonds—such as those in the Schiff base precursor—between the dopamine catechol moiety and gelatin molecules. In the healed state, the catechol structure reconstructs the crosslinking network through the reorganization of reversible hydrogen bonds, redox reactions, and the regeneration of dynamic covalent bonds with gelatin amino groups, thereby achieving interfacial fusion at the molecular level.

To evaluate the bioadhesive performance of Gel-PDA, this study conducted adhesion tests across multiple body sites (hand, elbow, knee, and finger) and various biological tissues (skin, heart, spleen, and liver). By comparing pre- and post-adhesion conditions, we systematically analyzed its adhesive adaptability and universality (Figure 5H). The results demonstrated that Gel-PDA maintained effective adhesion during dynamic processes such as hand extension and fist clenching, elbow flexion, knee morphological changes, and finger movements. This indicates its excellent adhesive stability on human soft tissues under dynamic mechanical stimuli, accommodating mechanical deformations and stresses induced by body motion. Furthermore, adhesion tests on biological tissues revealed that Gel-PDA could tightly conform to the surfaces of various tissue types, reflecting its universal adhesive capability across diverse biological substrates. The adhesion mechanism is mainly through the formation of a large number of hydrogen bonds, π–π stacking and other noncovalent interactions between the catechol group of polydopamine and the surface group of the tissue, as well as the formation of Schiff base covalent bonds with gelatin and other molecules under oxidative conditions to achieve strong wet adhesion. These findings provide an experimental basis for its potential applications in areas such as organ repair and tissue engineering scaffolds.

2.5 Biocompatibility evaluation of MN

Given that bacterial infection is a major contributor to delayed wound healing, we assessed the antimicrobial efficacy of MN patches. Notably, antimicrobial experiments were conducted using MNs composed of different materials. The results showed that bacteria grew normally around the Gel patch, as it lacked antibacterial components. In contrast, GelMA, GelMA-CSMA, GelMA-CS-β-CD-CSMA, and MN patches exhibited varying degrees of antimicrobial zones around them (Figure 6B), the inhibition zone of MN against *Staphylococcus aureus* reached 3.3 cm, which was significantly higher than that of the control group and the gelatin group ($P < 0.001$), confirming the antimicrobial properties of each material. Furthermore, the MN patch containing polymyxin effectively killed over 95% of *S aureus* and *Escherichia coli* in the cocultured bacterial suspension (Figure 6C), significantly higher than the control group ($P < 0.001$), demonstrating its exceptional antibacterial activity. This is attributed to the synergistic effect of CS in the tip part and polymyxin in the back part of the MN in this study. The puncture performance of the tip part physically penetrates the skin barrier and directly acts on the infected site. Polymyxin adsorbs and destroys the bacterial cell membrane by electrostatic adsorption, resulting in leakage of cell contents and rapid sterilization (Figure 6A). The results showed that MN could enhance the "breakthrough" and "resident" ability of drugs to the infection microenvironment in the infection model, showed a good preliminary bacteriostatic effect[51].

This efficacy is attributed to the synergistic coordination between polymyxin and CS, which endows the MNs with strong antibacterial effects, effectively inhibiting bacterial reproduction and growth.

Figure 6E, F illustrates that after incubation for the same duration, cell viability was comparable between the experimental

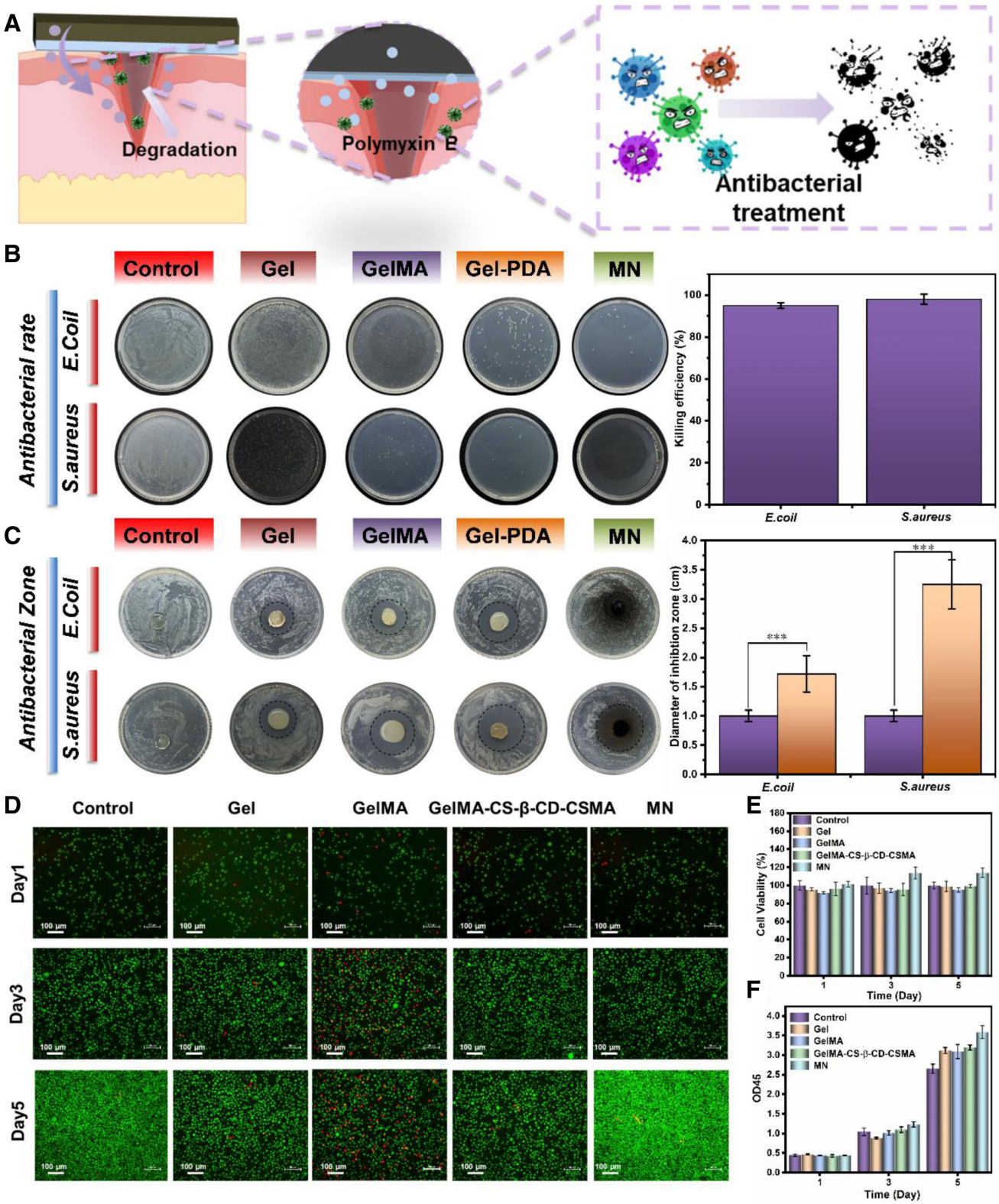

Figure 6. MN biocompatibility analysis. (A) Antibacterial Schematic of MN. (B) Plate counting method for E coli and S aureus of Control, Gel, GelMA, Gel-PDA, and MN. (C) Inhibition zone for E coli and S aureus of Control, Gel, GelMA, Gel-PDA, and MN. (D) Photomicrographs of the cell density of the MTT test of the Control, Gel, GelMA, GelMA-CS-β-CD-CSMA, and MN for 1, 3, and 5 days. (E) Changes in cell viability of Control, Gel, GelMA, GelMA-CS-β-CD-CSMA, and MN after 5 days of coculture with CHL cells. (F) Changes in OD45 of Control, Gel, GelMA, GelMA-CS-β-CD-CSMA, and MN after 5 days of coculture with CHL cells. Data are depicted as mean ± SD (n = 3) and analyzed by one-way ANOVA with Tukey's multiple comparison test compared to the control group. *P < 0.05, **P < 0.01, ***P < 0.001, and ****P < 0.0001 are statistically significant.

and control groups. On the 5th day, the cell activity in the MN group was significantly higher than that of the control group and exceeded the activity observed before treatment. This indicates that MN administration enhanced cellular activity and promoted cell growth and proliferation. Results from the Tetrazolium salt colorimetric assay (MTT) demonstrated that none of the experimental groups exhibited significant cytotoxicity (Figure 6D), as evidenced by robust cell growth and distribution on day 3. Notably, there were fewer, red-stained dead cells, and the number of green-stained cells in the MN group increased after 5 days, indicating that MN is biocompatible and promotes cell proliferation. These findings underscore the clinical potential of MN.

2.6 Evaluation of whole skin defect repair in animals of MN

Researchers have shown that skin lesions caused by BC have 2 main characteristics; difficulty in healing and long-term susceptibility to cancer[51], which necessitates the search for effective preventive and therapeutic measures. To evaluate the impact of MN on skin wound healing following BC surgery, we conducted in vivo testing to monitor the therapeutic efficacy of MN. This involved tracking changes in defective skin wounds and analyzing the associated histopathological changes in mice (Figure 7A). Rats were treated with 3 sets of MN patches, and Figure 7B displays the changes in skin wounds in mice after different treatments. When the treatment effects were applied to infected wound tissue, wound healing responses in the treatment group were less favorable from days 0 to 3. This was likely due to hemostatic occlusion caused by the MNs in the early stages, as well as minor cytotoxicity from the CS-β-CD NPs. At day 7, the skin wound area was significantly reduced in all treatment groups, and administration of GelMA, CSMA, and bFGF promoted angiogenesis and cell proliferation, enhancing the expression of wound healing. On day 14, the blank group showed the lowest degree of healing with 50.0% of the original wound area. Compared with the blank group, the GelMA-treated group showed a significant reduction in skin wound area. Notably, The healing rate was: MN group > GelMA-CS-β-CD-CSMA group > GelMA group > Control group (Figure 7C, D). In addition, at any time point, the wound area of rats in the MN group was the smallest among all groups, and the wound closure rate was higher than 95% after 14 days of treatment. The Gel-PDA backing part can reshape the typical inflammatory wound microenvironment into a repair-oriented immune homeostasis during wound healing. Its core is to actively regulate the immune response. bFGF fundamentally reverses the immune state that hinders healing by guiding macrophages to polarize from pro-inflammatory M1 to anti-inflammatory and pro-repairing M2, and reducing the level of local pro-inflammatory M2 and. At the same time, the hydrogel, as an "intelligent" delivery system, can respond to the wound environment, continuously and stably release bFGF, and accurately promote angiogenesis and cell proliferation; the dopamine component effectively scavenges reactive oxygen species, alleviates oxidative stress damage, and its potential antibacterial properties also prevent infection.

This is due to the fact that bEGF can stimulate the endogenous expression of fibroblasts and significantly promote cell proliferation, and the elevation of fibroblasts can directly promote the formation of collagen fibers and increase the connective tissues, which can enhance the antitensile strength of the wound and accelerate wound healing. Gel, CS, and growth factors synergistically accelerate vascularization in the wound, enabling the reconstruction of 90% new skin in a significantly shorter time. This indicated significant improvement in skin damage, demonstrating its effectiveness in repairing BC wounds.

To provide a more detailed comparison of microscopic changes within the wound, tissue sections were analyzed using immunofluorescence and pathological staining techniques. These included hematoxylin and eosin (H&E) staining, Masson's trichrome staining, and CD31 staining for platelet endothelial cell adhesion molecules. Figure 7E exhibits the micrographs of wound tissue sections of different treatments on day 14. Wound healing is observed by H&E staining. Masson staining reflects the growth of collagen fibers in the wound.CD-31 specifically stains platelet endothelial cell adhesion molecules and plays an important role in the interaction with neutrophils. Key elements in the photographic results, such as blood vessels, neutrophils, hair follicles, and collagen deposits within the wound area, were highlighted to facilitate observation and analysis. Compared with the control group, more mature collagen and sustained epithelial tissue production was observed in the MN group (Figure 7F, G). H&E staining showed the lowest number of neutrophils in the MN treatment group, indicating minimal wound inflammation. Masson staining showed more collagen fiber deposition in the treatment groups, especially in the MN treatment group, which had the densest collagen fiber deposition, and the deposition of collagen fibers was almost the same as that of intact skin. In addition, the expression of CD31 was higher in the treated group, and a higher number of fibroblasts, keratinocytes, granulation and re-epithelialization processes were observed in the area, in agreement with the results of H&E staining and Masson staining. Optimal wound repair was achieved through the combined effects of Gel, CS, and bFGF. This further confirms that MN demonstrates excellent biosafety and effectively promotes cell regeneration. The new smart MN can accelerate wound healing providing a new idea for clinical BC wounds that are difficult to heal.

2.7 Drug release and in vitro anticancer characterization of MN

Given the strong absorption peak of DOX at 481 nm (Figure 8C), this wavelength was selected for establishing its standard calibration curve. The linear relationship between the absorbance and concentration of DOX standard solutions is presented in Figure 8D. As shown in Figure 8E, the initial DOX solution exhibited significantly higher absorbance compared to the supernatant. Substituting the measured supernatant absorbance (0.140) into the standard curve yielded a supernatant DOX concentration (c1) of 6.5 μg/mL. Subsequently, the DOX loading capacity in the MN was calculated as 68.8% using Equation. This high loading efficiency is primarily attributed to the hydrophilic cyclodextrin structures on the surface of the CS-β-CD NPs. These cyclodextrins are closely packed, creating a hollow internal cavity that provides efficient space for DOX encapsulation.

$$\text{Loading factor} = (1 - c_1/c_2) \times 100\% = (1 - 6.5/20.83) \times 100\% = 68.8\%$$

Subsequently, the drug release profiles of DOX-CS-β-CD NPs and MN were examined separately in PBS at different pH values (Figure 8F, G). In pH 7.4 PBS, DOX-CS-β-CD NPs exhibited a sustained release profile, with cumulative release rates of 42% at 24 hour and 52% at 48 hour. In contrast, release was significantly accelerated in pH 5.5 PBS, reaching cumulative rates of 65.2% at 24 hour and 85.5% at 48 hour. This accelerated release is attributed to the acid-triggered destabilization of CS-β-CD NPs and the responsive disassembly of their crosslinked CS/TPP core regions (Figure 8A). Similarly, MN displayed pH-responsive release behavior, with DOX release significantly faster in pH 5.5 PBS compared to pH 7.4 (Figure 8G, H). However, drug release from MN was slightly delayed relative to that from the DOX-CS-β-CD NPs. This delay is likely due to the requirement for DOX to first be released from the NPs, then diffuse through the MN's 3D network structure driven by osmotic pressure before entering the release medium (Figure 8B).

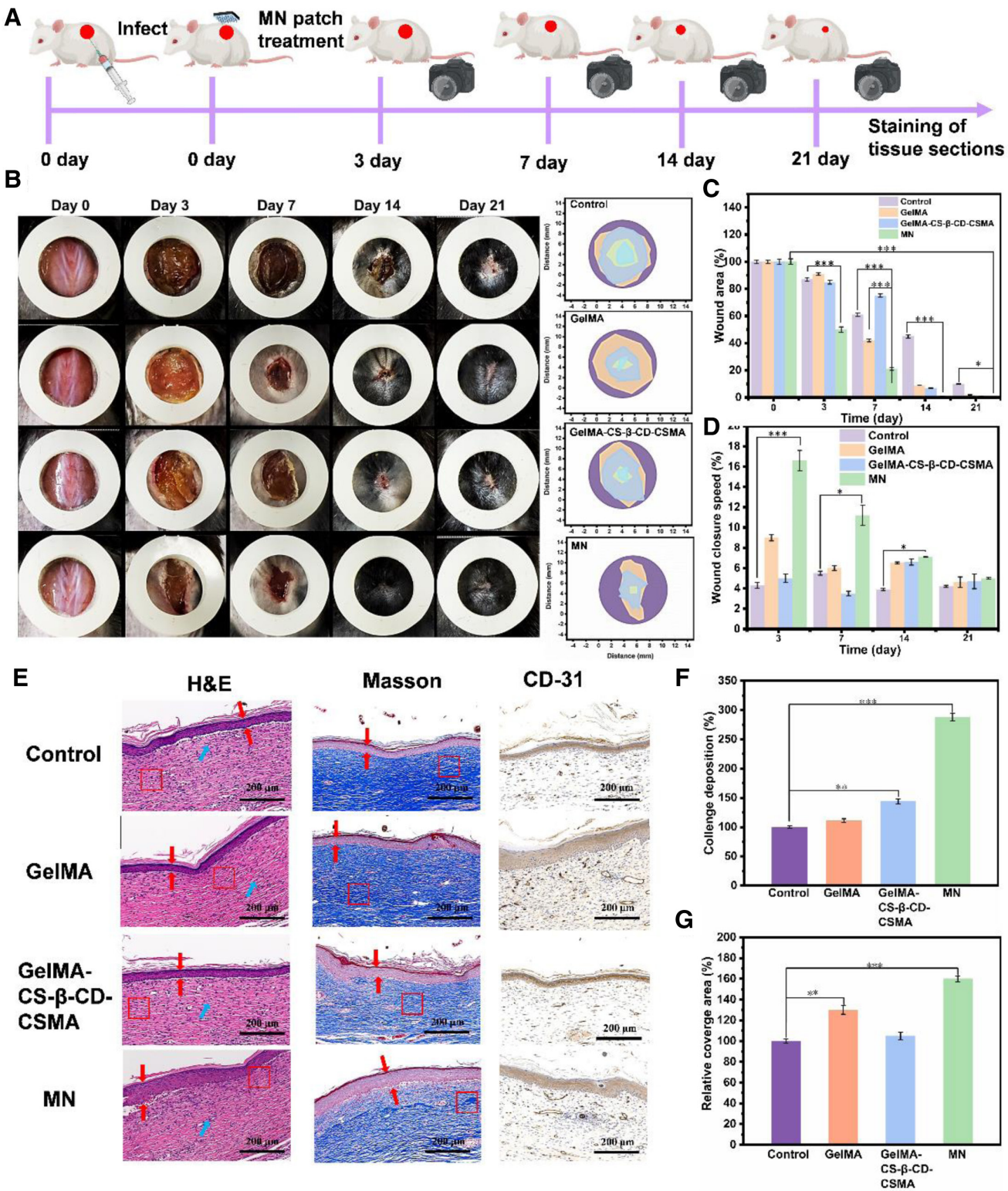

Figure 7. Repair of full-thickness skin defects in rats. (A) Schematic representation of wound formation and treatment in rats. (B) Representative images and description of wound healing on day 0, 3, 7, 14, and 21 after Control, GelMA, GelMA-CS-β-CD-CSMA and MN treatment. (C) Wound closure rate on day 0, 3, 7, 14, and 21. (D) Wound closure velocity rate on day 0, 3, 7, 14, and 21. (E) H&E staining, Masson staining and CD-31 staining of tissues on day 14. (F) Collagen deposition of regenerated skin tissue on day 21. (G) CD31 positive expression on day 14. Data are depicted as mean ± SD (n = 3) and analyzed by one-way ANOVA with Tukey's multiple comparison test compared to the control group. *P < 0.05, **P < 0.01, ***P < 0.001, and ****P < 0.0001 are statistically significant.

These results indicate that both DOX-CS-β-CD NPs and MN possess favorable pH-responsive drug release properties. MN can achieve programmed administration through pH response, demonstrating preliminary intelligent intervention in the TME. This "adaptive" treatment strategy is highly compatible with the cutting-edge nanomedicine concept[52].

The antitumor efficacy of different DOX formulations was evaluated using HeLa cells (Figure 8I). After 72-hour incubation, all

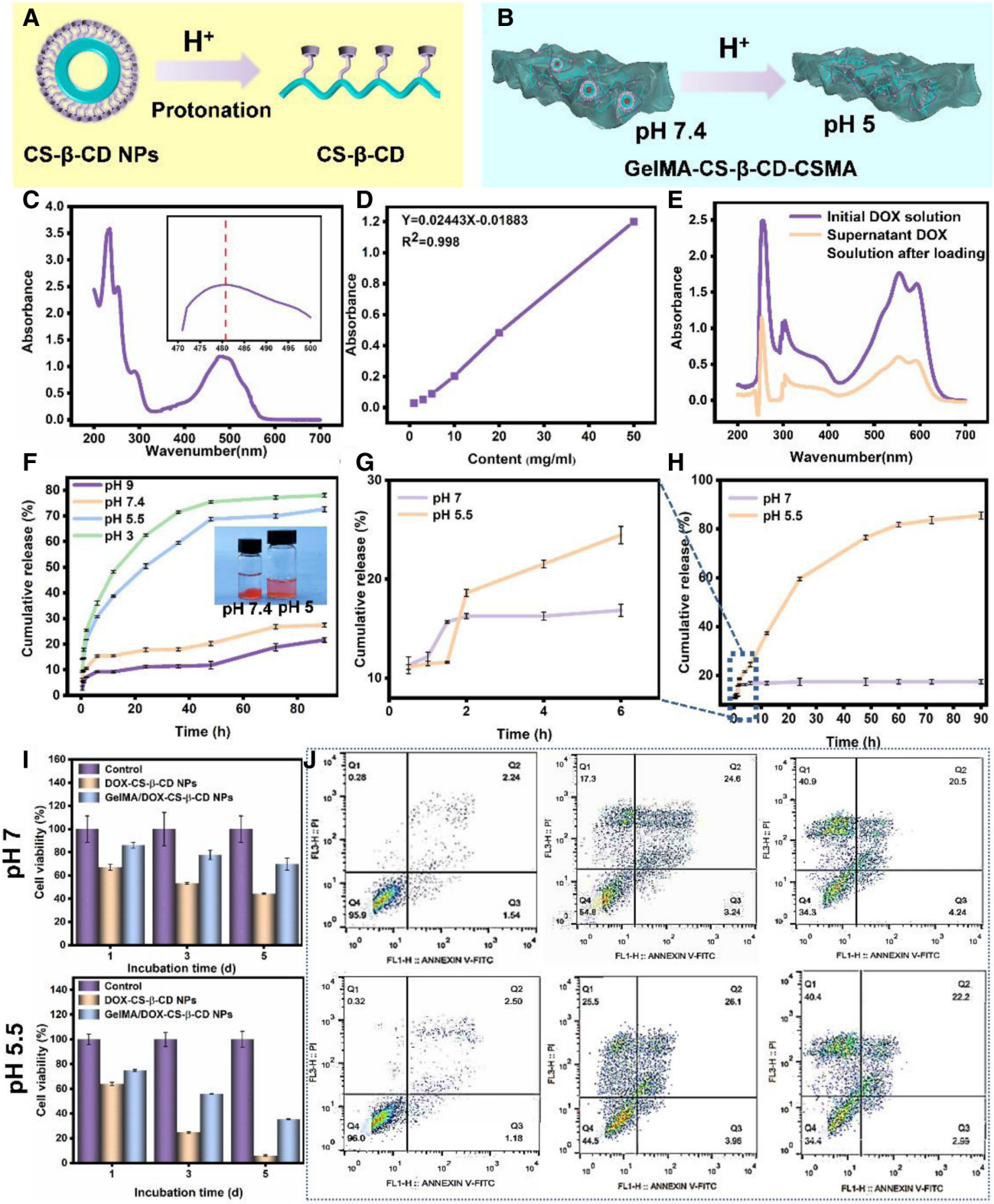

Figure 8. (A) pH-dependent dissociation mechanism of CS-β-CD NPs. (B) Schematic illustration of pH-responsive drug release from GelMA-CS-β-CD-CSMA hydrogel. (C) UV-vis absorption spectrum of DOX. (D) DOX concentration calibration curve. (E) Absorbance comparison of CS-β-CD NPs supernatant pre- and post-DOX loading. (F) The pH-dependent release profiles of DOX from CS-β-CD NPs in PBS within 96 hour. (G, H) The pH-responsive release kinetics of MN in PBS within 96 hour. (I) Comparative anticancer efficacy of DOX formulations under different pH conditions (5.5 and 7) on day 1, 3, and 5. (J) Apoptosis analysis of HeLa cells treated with DOX formulations for 48 h (flow cytometry). Data are depicted as mean ± SD (n = 3) and analyzed by one-way ANOVA with Tukey's multiple comparison test compared to the control group. *P < 0.05, **P < 0.01, ***P < 0.001, and ****P < 0.0001 are statistically significant.

treatment groups demonstrated significant proliferation inhibition compared to the control. Notably, GelMA/DOX-CS-β-CD NPs showed reduced cytotoxicity versus DOX-CS-β-CD NPs solution, with significantly enhanced inhibition at pH 5.5 versus pH 7.4. This pH-dependent effect correlates with accelerated drug release kinetics and higher cumulative release under acidic conditions, resulting in prolonged tumor suppression. The attenuated efficacy of GelMA/DOX-CS-β-CD NPs likely stems from: (1) slower drug release from the hydrogel matrix, and (2) potential cytoprotective effects of gelatin. These observations align with previous release profiles and biocompatibility data. Flow cytometry analysis (Figure 8J) revealed significantly increased apoptotic populations (Q2 + Q3 quadrants) at pH 5.5 versus pH 7.4, confirming enhanced pH-responsive cytotoxicity. These results collectively demonstrate the system's intelligent drug release capability and potent anticancer activity. To verify the DOX-specific inhibitory mechanism, we analyzed cellular uptake of DOX-CS-β-CD NPs and GelMA/DOX-CS-β-CD NPs in HeLa cells (Supplementary Figure 10, https://links.lww.com/MEDMAT/A8). Fluorescence imaging revealed distinct distribution patterns: free DOX showed nuclear and cytoplasmic localization, while nanocarrier-loaded DOX exhibited predominant cytoplasmic accumulation. This differential localization suggests distinct cellular internalization mechanisms – passive diffusion for free DOX versus likely receptor-mediated endocytosis for the nanocarrier systems[53]. The observed intracellular DOX accumulation confirms effective cellular entry and subsequent growth inhibition, supporting the DOX-dependent nature of the cytotoxic effects.

2.8 In vivo assessment of anticancer effects of MN

Next, we established a mouse model of BC to investigate the in vivo therapeutic effect of MN (Figure 9A). BC cells were inoculated subcutaneously on the back of the mice, and after 7 days of tumor formation, treatment was initiated, and the tumors were observed for 14 days. To confirm the protective effect of MN transdermal drug delivery on tumor recurrence in vivo, MNs without a tip portion (G1) and intact MNs with a tip portion (G2) were used to cover the wound for treatment. Figure 9B, C reveals that the tumor volume of mice in the blank group increased rapidly in a time-dependent manner, and the tumor growth was inhibited to some extent in the G1 group to a certain extent after the treatment, but the tumor growth resumed afterward. The present study employed DOX, a broad-spectrum anthracycline chemotherapeutic agent, In the acidic TME, DOX is rapidly released from the MN tips via a pH-triggered mechanism. While DOX directly eliminates rapidly proliferating tumor cells primarily by intercalating into DNA and inhibiting topoisomerase II, it can also induce immunogenic cell death. During this process, DOX prompts the release of damage-associated molecular patterns and tumor antigens from the dying cells, which in turn activates a systemic antitumor immune response—promoting the maturation of dendritic cells and recruiting cytotoxic T lymphocytes. Ultimately, this leads to the clearance of tumor cells by the activated immune system[54–57]. However, extensive evidence indicates that free DOX lacks selectivity in vivo due to its small molecular properties, enabling nonspecific systemic distribution via the enhanced permeability and retention effect and passive diffusion. This nontargeted distribution pattern not only results in rapid systemic dissemination but also leads to limited accumulation efficiency and short duration of therapeutic efficacy in tumor tissue. Consequently, the free DOX group failed to demonstrate significant tumor volume reduction in murine models[58–60]. Tumor size in the G2 group was significantly smaller relative to that of the control group and free DOX, which demonstrated that transdermal administration of MN prevented BC recurrence by ensuring the sustained release of the drug in the TME. In addition, the relative tumor volume and weight were recorded after 14 days (Figure 9D, E), and the tumor in the G2 group was well decreased, confirming that the drug-carrying tip of the MN specifically released DOX in the TME, effectively eliminating residual tumor and thereby preventing tumor recurrence. The spleen is an important site of extramedullary hematopoiesis, producing suppressor myeloid cells in tumor-bearing mice[61]. Studies have demonstrated a positive correlation between spleen weight and liver index and tumor weight[62]. Figure 9F shows that tumor recurrence was effectively controlled in the G2 group.

All collected tumor tissues and major organs were sectioned and stained with HE for histological analysis. In addition, GPX4 analysis and TUNEL analysis were performed on tumor tissues to assess tumor cell apoptosis[63]. The G1 and G2 groups induced more cancer cell damage, including vacuolization, necrosis, atrophy and cytoplasmic nuclear separation (Figure 10A). Furthermore, the degree of tumor necrosis was significantly higher in the G2 group compared to the G1 group. Immunofluorescence staining for GPX4 and TUNEL revealed a marked increase in the percentage of apoptotic tumor cells and greater cell death in the G1 group (Figure 10B, C). These findings collectively indicate that the growth of both primary and recurrent tumors was significantly inhibited.

DOX has been shown to have high antitumor efficacy in the treatment of various cancers, but its side effects, especially toxicity to major organs in circulation, should not be overlooked[62]. Studies have revealed that both intravenous and locally injected free DOX exhibit significant systemic toxicity due to its nonspecific distribution in vivo[64,65]. In contrast, in this experiment, the spleens of the treated and control mice were maintained at normal levels without significant damage. In addition, no significant toxicity was detected in major organs such as heart, liver, and kidney in the MN group based on histological section staining observations (Figure 10D). This further suggests that when DOX is delivered via MN, the drug is not diluted by entering the bloodstream and metabolized by the liver, but rather it enters the cancer tissues, which makes it safer by reducing the systemic toxicity of the drug. In conclusion, this MN is shown to be a promising local drug delivery system for the prevention of recurrence and distant metastasis after mastectomy of breast tumors.

3. Conclusions

In summary, we successfully developed a "smart response" MN system, which is an all-encompassing multifunctional treatment for metastatic BC and associated wound infections. MN combines nanotechnology with stimulus-responsive microneedling technology to introduce pH-responsive drug carriers in a photocrosslinked gelatin matrix capable of specifically releasing drugs for prolonged periods of time in the TME. Our proposed MN has a compact fibrous network structure, exhibits the ability to deliver therapeutic drugs locally by penetrating skin tissue, has excellent mechanical properties, antimicrobial properties, repairs damaged tissues, and inhibits the recurrence of BC, and can provide comprehensive data to guide clinical practice. Noteworthy: to improve the application of MN in postoperative trauma repair of BC, we designed a 2-stage MN based on the structure of MNs. The key advantage of this structure is that the needle tip can selectively release anticancer drugs in response to the TME, effectively targeting BC recurrence. Meanwhile, the substrate gradually releases bFGF and polymyxin over an extended period, thereby inhibiting inflammation and promoting angiogenesis and cell proliferation. Our results suggest that the MN can be used as a novel material for skin repair after BC surgery and wound infections, with a good safety profile.

4. Experimental

The detailed description of materials and methods can be found in the Supplementary Data File, https://links.lww.com/MEDMAT/A8.

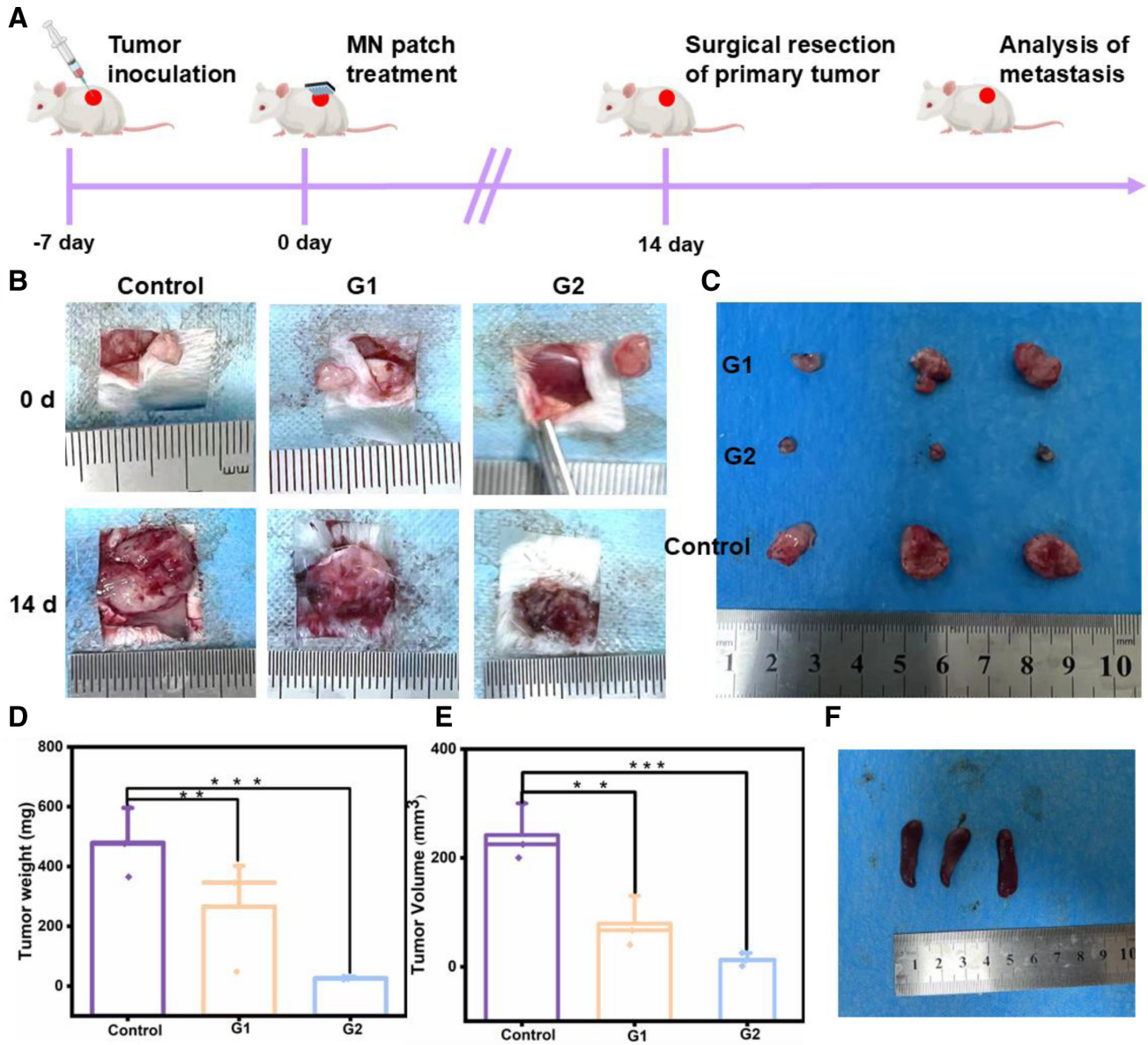

Figure 9. The antitumor effect in vivo was evaluated after 14 days of MN treatment. (A) Schematic diagram of in situ 4T1 tumor mice treatment. (B, C) The appearance of tumor tissue in Control, G1 and G2 on day 0 and 14. (D) Tumor weight records of Control, G1 and G2 on day 14. (E) Tumor volume records of Control, G1 and G2 on day 14. (F) Photographs of spleens of Control, G1 and G2 on day 14. G1: MN without a tip portion, G2: MN with a tip portion. Data are depicted as mean ± SD (n = 3) and analyzed by one-way ANOVA with Tukey's multiple comparison test compared to the control group. $^{*}P < 0.05$, $^{**}P < 0.01$, $^{***}P < 0.001$, and $^{****}P < 0.0001$ are statistically significant.

4.1 Data analysis

Materials and methods are described in Supplementary Information, https://links.lww.com/MEDMAT/A8. All data are depicted as mean ± standard deviation (n = 3), and significant differences were analyzed using OriginPro 2018 via one-way analysis of variance (ANOVA). The value of $P < 0.05$ was considered statistically significant ($^{*}P < 0.05$, $^{**}P < 0.01$, $^{***}P < 0.001$).

Acknowledgments

This work was financially supported by the National Natural Science Foundation of China (Grant Nos. 22278257, 22578259, and 12202323), the Fellowship of China Postdoctoral Science Foundation (Grant No. 2021M692000), the Key R&D Program of Shaanxi Province (Grant No. 2022GY–272), the Scientific ResearchPlan Projects of the Shaanxi Education Department (Grant No. 22JY013), and the Open Foundation of Key Laboratory of Auxiliary Chemistry and Technology for Chemical Industry, Ministry of Education, Shaanxi University of Science and Technology, Shaanxi Collaborative Innovation 28 Center of Industrial Auxiliary Chemistry and Technology, Shaanxi University of Science and Technology (Grant No. KFKT2022-11). The researchers would like to express their sincere gratitude to the Institute of Biomass & Functional Materials of Shaanxi University of Science and Technology for funding this research work. The tumor cell skin tissue in the image and some cartoon images are created by using the resources by Figdraw (www.figdraw.com).

Statement of ethics

Animal welfare was carried out strictly in accordance with the guide for the care and use of laboratory animals (Shaanxi

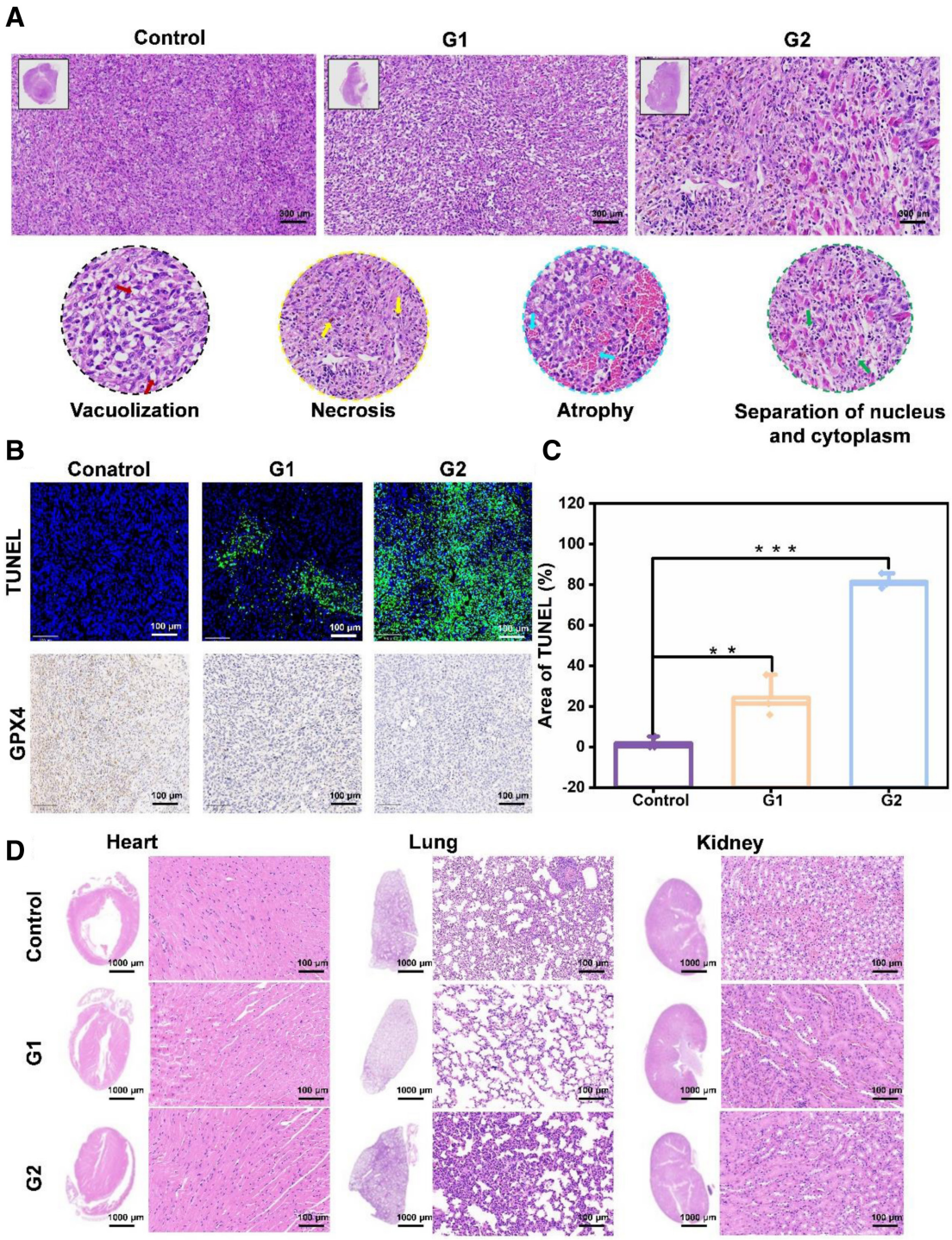

Figure 10. (A) On day 14 of treatment, H&E staining of tumor sections from different groups of mice with vacuolization in the cell (red arrowheads), cell necrosis (yellow arrowheads), cell atrophy (blue arrowheads), and separation of nucleus and cytoplasm (green arrowheads). (B) Immunohistochemical staining of TUNEL and GPX4 after 14 days of tumor treatment. (C) Area of TUNEL-positive zone after the 14th day of tumor treatment. (D) On day 14 of treatment, Cardiac, pulmonary, and renal toxicity profiles. G1: MN without a tip portion, G2: MN with a tip portion. Data are depicted as mean ± SD (n = 3) and analyzed by one-way ANOVA with Tukey's multiple comparison test compared to the control group. *P < 0.05, **P < 0.01, ***P < 0.001, and ****P < 0.0001 are statistically significant.

Province Science and Technology Department of China, SYXK [SHAN] 2021-008) and the related ethical regulations of the Institute for Hygiene of Ordnance Industry. All efforts were made to minimize animal suffering and to reduce the number of animals used. All participants were provided with information regarding the study and gave their written informed consent before participation.

Conflicts of interests

The authors declare that they have no conflicts of interest.

Data availability statement

The data that support the findings of this study are available from the corresponding author upon reasonable request.

Author contributions

Xinhua Liu and Yifan Fei conceived and designed the research. Yifan Fei and Xing Chen conducted the experiment. Xing Chen and Meilun Zhai supported the experiments. Ling Wen and Meilun Zhai conducted animal experiments and guided Yifan Fei analysis. Yifan Fei wrote the manuscript under the supervision of Xinhua Liu and Huie Jiang. Ouyang Yue and revised and embellished the manuscript. Xuechuan Wang and Xinhua Liu provided financial support. All authors were involved in the discussion and finalization of the manuscript. We confirm that all authors have read and approved the manuscripts.

References

[1] Poudel AJ, He F, Huang L, et al. Supramolecular hydrogels based on poly (ethylene glycol)-poly (lactic acid) block copolymer micelles and α-cyclodextrin for potential injectable drug delivery system. *Carbohydr Polym*. 2018;194:69–79.

[2] Bellefroid C, Lechanteur A, Evrard B, et al. In vitro skin penetration enhancement techniques: a combined approach of ethosomes and microneedles. *Int J Pharm*. 2019;572:118793.

[3] Cao C, Yang N, Zhao Y, et al. Biodegradable hydrogel with thermoresponse and hemostatic effect for photothermal enhanced anti-infective therapy. *Nano Today*. 2021;39:101165.

[4] Chen J, Zhang X, Zhang J, et al. Multifunctional hydrogel for synergistic reoxygenation and chemo/photothermal therapy in metastatic breast cancer recurrence and wound infection. *J Control Release*. 2024;365:74–88.

[5] Heng C, Peng X, Luo Y, et al. A photocrosslinked methacrylated carboxymethyl chitosan/oxidized locust bean gum double network hydrogel for cartilage repair. *J Mater Chem B*. 2023;11(43):10464–10481.

[6] Cheng X, Yang Y, Liao Z, et al. Drug-loaded mucoadhesive microneedle patch for the treatment of oral submucous fibrosis. *Front Bioeng Biotechnol*. 2023;11:1251583.

[7] Chhabra A, Prabhakar H, Subramaniam R, et al. Paravertebral anesthesia with or without sedation versus general anaesthesia for women undergoing breast cancer surgery. *Cochrane Database Syst Rev*. 2021;25(2):CD012968.

[8] Cruceriu D, Baldasici O, Berindan-Neagoe I. The dual role of tumor necrosis factor-alpha (TNF-α) in breast cancer: molecular insights and therapeutic approaches. *Cell Oncol (Dordr)*. 2020;43(1):1–18.

[9] Deshkar SS, Jadhav MS, Shirolkar SV. Development of carbamazepine nanostructured lipid carrier loaded thermosensitive gel for intranasal delivery. *Adv Pharm Bull*. 2021;11(1):150–162.

[10] Ding H, Tan P, Fu S, et al. Preparation and application of pH-responsive drug delivery systems. *J Control Release*. 2022;348:206–238.

[11] Duong HTT, Yin Y, Thambi T, et al. Smart vaccine delivery based on microneedle arrays decorated with ultra-pH-responsive copolymers for cancer immunotherapy. *Biomaterials*. 2018;185:13–24.

[12] Fan R, Sun W, Zhang T, et al. Paclitaxel-nanocrystals-loaded network thermosensitive hydrogel for localised postsurgical recurrent of breast cancer after surgical resection. *Biomed Pharmacother*. 2022;150:113017.

[13] Han B, Zheng R, Zeng H, et al. Cancer incidence and mortality in China. *J Natl Cancer Cent*. 2024;4(1):47–53.

[14] Hao Y, Chen Y, He X, et al. Near-infrared responsive 5-fluorouracil and indocyanine green loaded MPEG-PCL nanoparticle integrated with dissolvable microneedle for skin cancer therapy. *Bioact Mater*. 2020;5:542–552.

[15] Howard-Anderson J, Ganz PA, Bower JE, et al. Quality of life, fertility concerns, and behavioral health outcomes in younger breast cancer survivors: a systematic review. *J Natl Cancer Inst*. 2012;104(5):386–405.

[16] Hu T, Gong H, Xu J, et al. Nanomedicines for overcoming cancer drug resistance. *Pharmaceutics*. 2022;14(8):1606.

[17] Jeon EY, Lee J, Kim BJ, et al. Bio-inspired swellable hydrogel-forming double-layered adhesive microneedle protein patch for regenerative internal/external surgical closure. *Biomaterials*. 2019;222:119439.

[18] Jiang W, Li Y, Zhang S, et al. Association between cellular immune response and spleen weight in mice with hepatocellular carcinoma. *Oncol Lett*. 2021;22(2):625.

[19] Khan S, Hasan A, Attar F, et al. Diagnostic and drug release systems based on microneedle arrays in breast cancer therapy. *J Control Release*. 2021;338(338):341–357.

[20] Kong X, Cheng R, Wang J, et al. Nanomedicines inhibiting tumor metastasis and recurrence and their clinical applications. *Nano Today*. 2021;36:101004–101004.

[21] Lee KJ, Jeong SS, Roh DH, et al. A practical guide to the development of microneedle systems-In clinical trials or on the market. *Int J Pharm*. 2020;573:118778.

[22] Li Q, Wen J, Liu C, et al. Graphene-nanoparticle-based self-healing hydrogel in preventing postoperative recurrence of breast cancer. *ACS Biomater Sci Eng*. 2019;5(2):768–779.

[23] Li S, Wang X, Zhang Y, et al. Microneedle patches with antimicrobial and immunomodulating properties for infected wound healing. *Adv Sci*. 2023;10(22):e2300576.

[24] Liang Y, Zhang H, Song X, et al. Metastatic heterogeneity of breast cancer: molecular mechanism and potential therapeutic targets. *Semin Cancer Biol*. 2020;60:14–27.

[25] Lin Z, Gao W, Hu H, et al. Novel thermo-sensitive hydrogel system with paclitaxel nanocrystals: high drug-loading, sustained drug release and extended local retention guaranteeing better efficacy and lower toxicity. *J Control Release*. 2014;174:161–170.

[26] Liu B, Wang Y, Miao Y, et al. Hydrogen bonds autonomously powered gelatin methacrylate hydrogels with super-elasticity, self-heal and underwater self-adhesion for sutureless skin and stomach surgery and E-skin. *Biomaterials*. 2018;171:83–96.

[27] Liu D, Zhang Y, Jiang G, et al. Fabrication of dissolving microneedles with thermal-responsive coating for NIR-triggered transdermal delivery of metformin on diabetic rats. *ACS Biomater Sci Eng*. 2018;4:1687–1695.

[28] Liu L, Li X, Shi X, et al. Injectable alendronate-functionalized GelMA hydrogels for mineralization and osteogenesis. *RSC Adv*. 2018;8:22764–22776.

[29] Liu S, Jin M, Quan Y, et al. The development and characteristics of novel microneedle arrays fabricated from hyaluronic acid, and their application in the transdermal delivery of insulin. *J Control Release*. 2012;161:933–941.

[30] Liu Y, He C, Qiao T, et al. Coral-inspired hollow microneedle patch with smart sensor therapy for wound infection. *Adv Funct Mater*. 2024;34:2470131.

[31] Liu Y, Li C, Xia H, et al. An injectable superior depot of telratolimod inhibits post-surgical tumor recurrence and distant metastases. *Acta Biomater*. 2022;141:132–139.

[32] McAlister E, Kirkby M, Domínguez-Robles J, et al. The role of microneedle arrays in drug delivery and patient monitoring to prevent diabetes induced fibrosis. *Adv Drug Deliv Rev*. 2021;175:113825.

[33] Men K, Huang R, Zhang X, et al. Local and systemic delivery of interleukin-12 gene by cationic micelles for cancer immunogene therapy. *J Biomed Nanotechnol*. 2018;14(10):1719–1730.

[34] Meng Y, Li XJ, Li Y, et al. Novel double-layer dissolving microneedles for transmucosal sequential delivery of multiple drugs in the treatment of oral mucosa diseases. *ACS Appl Mater Interfaces*. 2023;15(11):13892–13906.

[35] Nuutila K, Samandari M, Endo Y, et al. In vivo printing of growth factor-eluting adhesive scaffolds improves wound healing. *Bioact Mater*. 2021;8:296–308.

[36] O'Connell RL, Rusby JE. Efficacy of prophylactic antibiotic administration for breast cancer surgery in overweight or obese patients: research highlight. *Gland Surg*. 2013;2(2):107–109.

[37] Oktay K, Harvey BE, Partridge AH, et al. Fertility preservation in patients with cancer: ASCO clinical practice guideline update. *J Clin Oncol*. 2018;36:1994–2001.

[38] Pan A, Wang Z, Chen B, et al. Localized co-delivery of collagenase and trastuzumab by thermosensitive hydrogels for enhanced antitumor efficacy in human breast xenograft. *Drug Deliv*. 2018;25(1):1495–1503.

[39] Kang RH, Kim Y, Kim JH, et al. Self-activating therapeutic nanoparticle: a targeted tumor therapy using reactive oxygen species self-generation and switch-on drug release. *ACS Appl Mater Interfaces*. 2021;13(26):30359–30372.

[40] Tellini R, Antonelli A, Tardanico R, et al. Positive surgical margins predict progression-free survival after nephron-sparing surgery for renal cell carcinoma: results from a single center cohort of 459 cases with a minimum follow-up of 5 years. *Clin Genitourin Cancer*. 2019;17(1):e26–e31.

[41] Rosenthal A, Israilevich R, Moy R. Management of acute radiation dermatitis: a review of the literature and proposal for treatment algorithm. *J Am Acad Dermatol*. 2019;81(2):558–567.

[42] Samant PP, Prausnitz MR. Mechanisms of sampling interstitial fluid from skin using a microneedle patch. *Proc Natl Acad Sci U S A*. 2018;115(18):4583–4588.

[43] Sullivan SP, Koutsonanos DG, Del Pilar Martin M, et al. Dissolving polymer microneedle patches for influenza vaccination. *Nat Med*. 2010;16(8):915–920.

[44] Vitorino C, Almeida J, Gonçalves LM, et al. Co-encapsulating nanostructured lipid carriers for transdermal application: from experimental design to the molecular detail. *J Control Release*. 2013;167(3):301–314.
[45] Waghule T, Singhvi G, Dubey SK, et al. Microneedles: a smart approach and increasing potential for transdermal drug delivery system. *Biomed Pharmacother*. 2019;109:1249–1258.
[46] Wang C, He G, Zhao H, et al. Enhancing deep-seated melanoma therapy through wearable self-powered microneedle patch. *Adv Mater*. 2024;36(11):e2311246.
[47] Williams AC, Barry BW. Penetration enhancers. *Adv Drug Deliv Rev*. 2004;56(5):603–618.
[48] Wu C, Ning H, Liu M, et al. Spleen mediates a distinct hematopoietic progenitor response supporting tumor-promoting myelopoiesis. *J Clin Invest*. 2018;128(8):3425–3438.
[49] Wu Y, Wang H, Gao F, et al. An injectable supramolecular polymer nanocomposite hydrogel for prevention of breast cancer recurrence with theranostic and mammoplastic functions. *Adv Funct Mater*. 2018;28(21):1801000.
[50] Chu Z, Zheng W, Fu W, et al. Implanted microneedles loaded with sparfloxacin and zinc-manganese sulfide nanoparticles activates immunity for postoperative triple-negative breast cancer to prevent recurrence and metastasis. *Adv Sci (Weinh)*. 2025;12(16):e2416270.
[51] Xiao S, Xie L, Gao Y, et al. Artificial phages with biocatalytic spikes for synergistically eradicating antibiotic-resistant biofilms. *Adv Mater*. 2024;36:2404411.
[52] Gao Y, Deng Y, Geng W, et al. Infectious and inflammatory microenvironment self-adaptive artificial peroxisomes with synergetic co-ru pair centers for programmed diabetic ulcer therapy. *Adv Mater*. 2024;36:2408787.
[53] Wu Y, Yao Y, Zhang J, et al. Tumor-targeted injectable double-network hydrogel for prevention of breast cancer recurrence and wound infection via synergistic photothermal and brachytherapy. *Adv Sci*. 2022;9(24):e2200681.
[54] Lei H, Wang X, Wu C. Early stage intercalation of doxorubicin to DNA fragments observed in molecular dynamics binding simulations. *J Mol Graph Model*. 2012;38:279–289.
[55] Soliman TN, Keifenheim D, Parker PJ, et al. Cell cycle responses to Topoisomerase II inhibition: molecular mechanisms and clinical implications. *J Cell Biol*. 2023;222(12):e202209125.
[56] Silva GER, Padovezi ACE, Barzotti RJ, et al. Induction of oxidative stress and functional impairment by Doxorubicin in rat salivary glands. *Naunyn Schmiedebergs Arch Pharmacol*. 2025.
[57] Xie Y, Li K, Liang J, et al. Co-delivery of doxorubicin and STING agonist cGAMP for enhanced antitumor immunity. *Int J Pharm*. 2024;654:123955.
[58] Lin YT, Meng R, Zhang SM, et al. Acid-responsive biocompatible hydrogel modulating tumor DNA self-repair collaborated with chemotherapy for boosting STING pathway-associated immunotherapy. *Nano Lett*. 2025;25(9):3670–3680.
[59] Luo X, Liu Z, Fang S, et al. Implantable hydrogel-based scaffold integrating cascaded chemotherapy and self-amplified immunotherapy to suppress postsurgical tumor recurrence. *J Colloid Interface Sci*. 2025;700(Pt 2):138475.
[60] Gong Y, Yuan W, Liu S, et al. Physical encapsulation and chemotherapy: a synergistic hydrogel strategy for tumor suppression. *Adv Healthc Mater*. 2025;14(20):e2500511.
[61] Yang X, Gao L, Wei Y, et al. Photothermal hydrogel platform for prevention of post-surgical tumor recurrence and improving breast reconstruction. *J Nanobiotechnology*. 2021;19:307.
[62] Zhang Z, Cao Q, Xia Y, et al. Combination of biodegradable hydrogel and antioxidant bioadhesive for treatment of breast cancer recurrence and radiation skin injury. *Bioact Mater*. 2023;31:408–421.
[63] Xue H, Jin J, Huang X, et al. Wearable flexible ultrasound microneedle patch for cancer immunotherapy. *Nat Commun*. 20256:2650.
[64] Zhao X, Liu S, Yildirimer L, et al. Injectable stem cell-laden photocrosslinkable microspheres fabricated using microfluidics for rapid generation of osteogenic tissue constructs. *Adv Funct Mater*. 2016;26(17):2809–2819.
[65] Zhao Z, Chen Y, Shi Y. Microneedles: a potential strategy in transdermal delivery and application in the management of psoriasis. *RSC Adv*. 2020;10(24):14040–14049.

How to cite this article: Fei Y, Liu X, Zhai M, Chen X, Yue O, Wang X, Jiang H, Chen Y. A two-stage nanoengineered microneedle platform for on-demand tumor-microenvironment-responsive therapy and enhanced wound healing against postoperative breast cancer recurrence. MedMat 2026;3(1):e00035. doi: 10.1097/mm9.0000000000000035